Search for an Eta-Nuclear Bound State in the Double Charge Exchange Reaction $^{18}O(\pi^+, \pi^-)^{18}Ne$ (DIAS)

*John Doeppers Johnson**

Guest Scientist at Los Alamos Group MP-10.
Department of Physics, University of Texas at Austin, Austin, TX 78712-1081

Los Alamos

NATIONAL LABORATORY

Los Alamos, New Mexico 87545

MASTER

Acknowledgments

I would like to thank my advisor, Dr. C. Fred Moore for his patience and support during my years as a graduate student at The University of Texas. I would also like to thank my many friends and colleagues who were instrumental and supportive throughout my college career. I would like to extend a special thanks to Dr. Christopher Morris, he has taught me a great deal about experimental methods and has provided a great deal of guidance. I have worked closely with many people at LAMPF and NSCL who have helped me in my understanding and appreciation of physics. I extend my wholehearted thanks to Allen Williams, Mohini Rawool-Sullivan, John O'Donnell, John Zumbro, Peter Riley, George Burleson, George Glass, Lon-Chang Liu, Jerry Nolen, Al Zeller, Brad Sherril, Felix Marti and many more.

SEARCH FOR AN ETA-NUCLEAR BOUND STATE IN THE DOUBLE CHARGE EXCHANGE REACTION $^{18}O(\pi^+, \pi^-)^{18}Ne(DIAS)$

by

John Doeppers Johnson

ABSTRACT

Recent calculations have predicted that a bound state between an eta and a nucleus may occur as an intermediate state in pion double charge exchange (DCX). The existence of such a mesic nucleus would lead to a resonance-like structure in the DCX excitation function at fixed momentum transfer. LAMPF Experiment 1140 searched for an η-nucleus bound state in the DCX reaction $^{18}O(\pi^+, \pi^-)^{18}Ne(DIAS)$. An excitation function for this reaction was measured for energies ranging from 350 to 440 MeV and for momentum transfers of $q = 0$, 105 and 210 MeV/c. The calculated cross sections agree favorably with previously published data. Theoretical calculations predict that a resonance structure will be evidenced by an enhanced cross section at the eta production threshold for this reaction. The measured excitation function has found some evidence of structure in this region.

Table of Contents

List of Figures

List of Tables

Chapter 1

Introduction

In the search for new forms of nuclear matter it has become com-
monplace to study bound state systems. By observing sharp resonances in the
neutron capture reaction, nuclear levels at high excitation energy were found
to be much denser than first suspected [Bo-69]. Studies of the neutron bound
state also helped in the understanding of the compound nucleus. The possibil-
ity of the formation of η−nucleus bound states have been studied recently by
Haider and Liu [Ha-87]. It has been shown [Ha-86, Bh-86] that the low-energy
ηN interaction is attractive for A>10. Since the η is neutral, the Coulomb
effect does not contribute to this potential, and the η is bound to nucleons in
the nucleus by the strong force. In a similar manner to neutron capture, which
leads to the formation of a compound nucleus, it is believed that resonances
corresponding to an η bound state will be observed in pion double charge ex-
change (DCX) reactions. The η production threshold for most nuclei occurs
above an incident pion kinetic energy of $T_\pi \approx 400$ MeV. At this threshold the
η can be bound into the first nuclear orbital and a resonance effect should be
evidenced in the energy dependence of the cross section [Ha-87].

1.1 Pion Double Charge Exchange Reactions

There are several reasons that the pion is an ideal nuclear probe. The pion is the lightest meson and is therefore the mediator of the strong nuclear force [Yu-35]. To first order, the pion is assumed to interact with individual nucleons [Gi-85a]. The pion can be absorbed in nuclei and comes in three charge states, this makes the pion ideal for scattering and charge exchange reactions. Some properties of the pion are listed below [Pr-90].

$\pi^{\pm}$ Mass $= 139.5675 \pm 0.0004$ MeV
Mean Life $\tau = (2.6030 \pm 0.0024) \times 10^{-8}s$
$c\tau = 7.804$ m
Isospin T $= 1$, $T_z(\pi^+, \pi^-) = (1, -1)$
Spin $J^{\pi} = 0^-$, pseudoscalar

π° Mass $= 134.9739 \pm 0.0006$ MeV
Mean Life $\tau = (8.4 \pm 0.6) \times 10^{-17}s$
$c\tau = 2.5 \times 10^{-6}$ m
Isospin T $= 1$, $T_z(\pi^{\circ}) = (0)$
Spin $J^{\pi} = 0^-$, pseudoscalar

Pion double charge exchange (DCX) reactions involve the transition from an initial state with (Z,N) nucleons to a final state with (Z±2,N∓2) nucleons.

$$\pi^{\pm}\ {}^{A}N_Z \rightarrow \pi^{\mp}\ {}^{A}N_{Z\pm2} \tag{1.1}$$

The final state is the double isobaric analog state (DIAS) of the initial state and has an identical wavefunction except for the T_z component of isospin. Fig. 1.1 shows graphically the isospin rules for pion-nucleus scattering reactions. Double charge exchange reactions can be considered to be two sequential single charge exchange (SCX) reactions. Each SCX step can be considered a generalization of the quasifree $\pi N \rightarrow \pi' N'$ process [Wi-91].

Pion - Nucleus Scattering
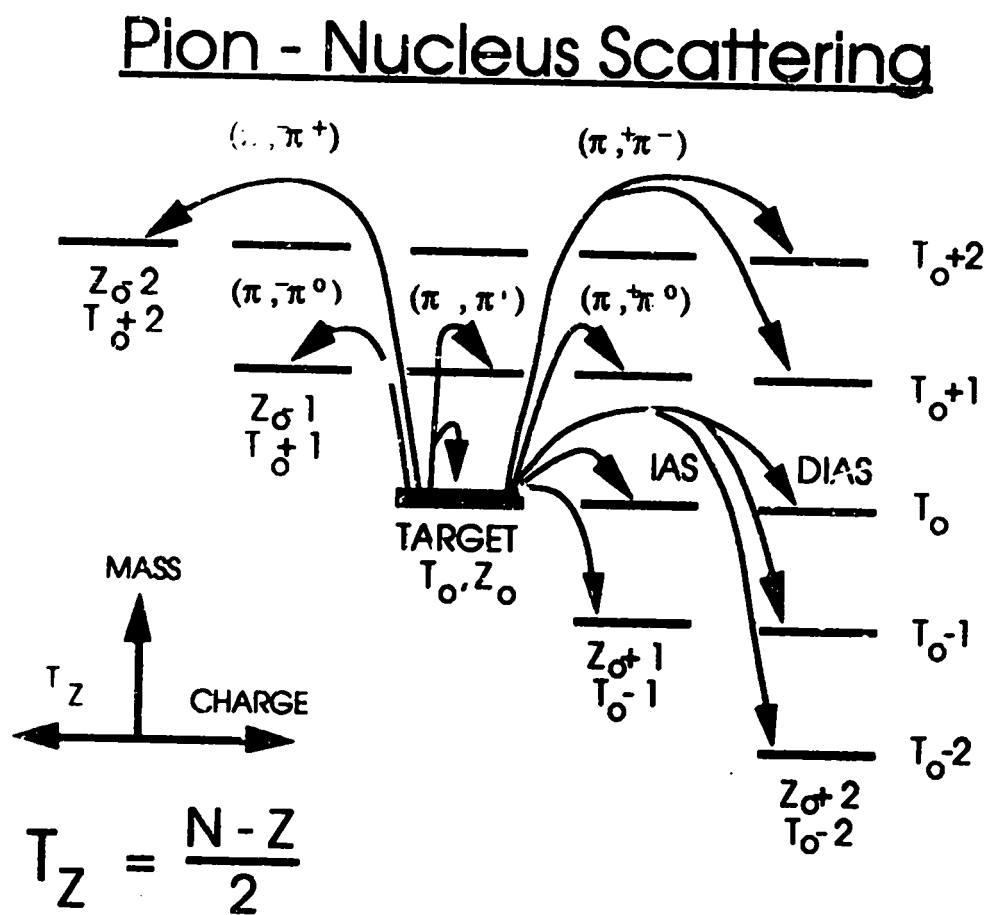
Figure 1.1: Isospin selection rules for pion-nucleus scattering.

1.2 Eta-Nuclear Bound States in DCX reactions

The two primary channels for pion double charge exchange reactions above $T_\pi \approx 400$ MeV are $\pi^+ \rightarrow \pi^\circ \rightarrow \pi^-$ and $\pi^+ \rightarrow \eta \rightarrow \pi^-$. The π° is in the continuum for this process, whereas the η can exist in the continuum or in a strongly bound nuclear state. Fig. 1.2 shows the analog and non-analog transition diagram and reaction mechanisms [Ha-87] for the channel $\pi^+ \rightarrow \pi^\circ \rightarrow \pi^-$. Fig. 1.3 shows the analog and non-analog transition diagrams and reaction mechanisms [Ha-87] for the channel $\pi^+ \rightarrow \eta \rightarrow \pi^-$. The excitation function for continuum mesons should be smoothly varying, whereas for a nuclear bound state the excitation function should show an enhancement. Calculations have been made which predict a resonance at 419 MeV for a momentum transfer of $q = 210$ MeV/c for the reaction $^{14}C(\pi^+,\pi^-)^{14}O(DIAS)$ [Ha-87]. This resonance should occur with a width of approximately 10 MeV and a fluctuation ratio, $R \sim 79\%$, where,

$$R = (\sigma_{max} - \sigma_{min})/\sigma_{average}. \tag{1.2}$$

Fig. 1.4 shows the theoretically predicted excitation functions for momentum transfers of $q = 0$ and 210 MeV/c for DCX on ^{14}C, with the smoothly varying background represented by a dashed line. Because the shell configuration for ^{18}O has two neutrons outside of the closed 1p shell, the level densities for higher excitation states is greater than that for ^{14}C and therefore it is predicted that a resonance effect would have a larger width and smaller fluctuation ratio [Li-92]. Fig 1.5 compares the ^{14}C and ^{18}O shell structures.

Experiment 1140 used the P^3—East energetic pion channel at the Clinton P. Anderson Meson Physics Facility (LAMPF) for measurements of
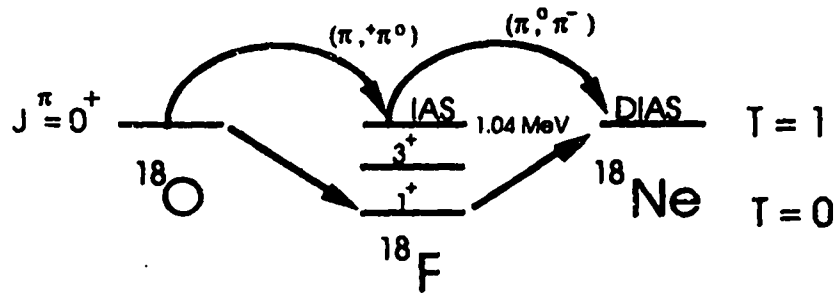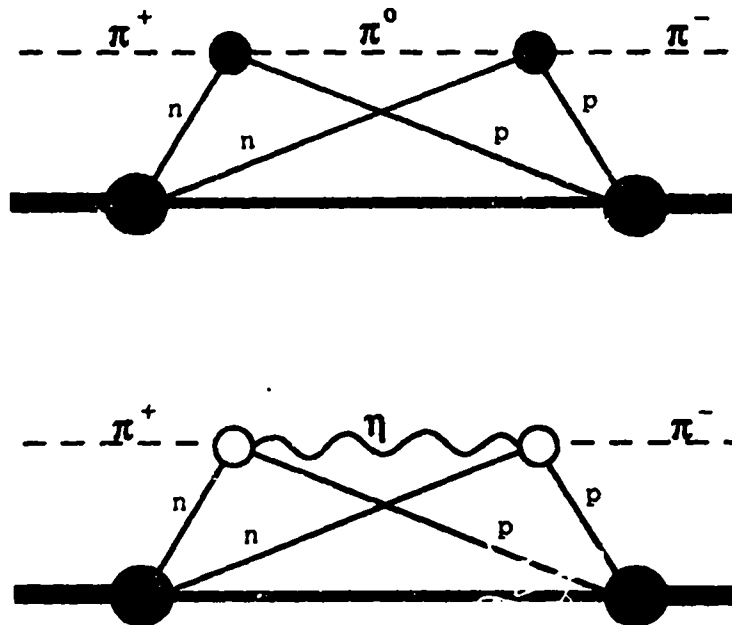
Figure 1.2: Analog and non-analog transition diagram and reaction mechanisms for $^{18}O(\pi^+,\pi^-)^{18}Ne(DIAS)$ [Ha-87].
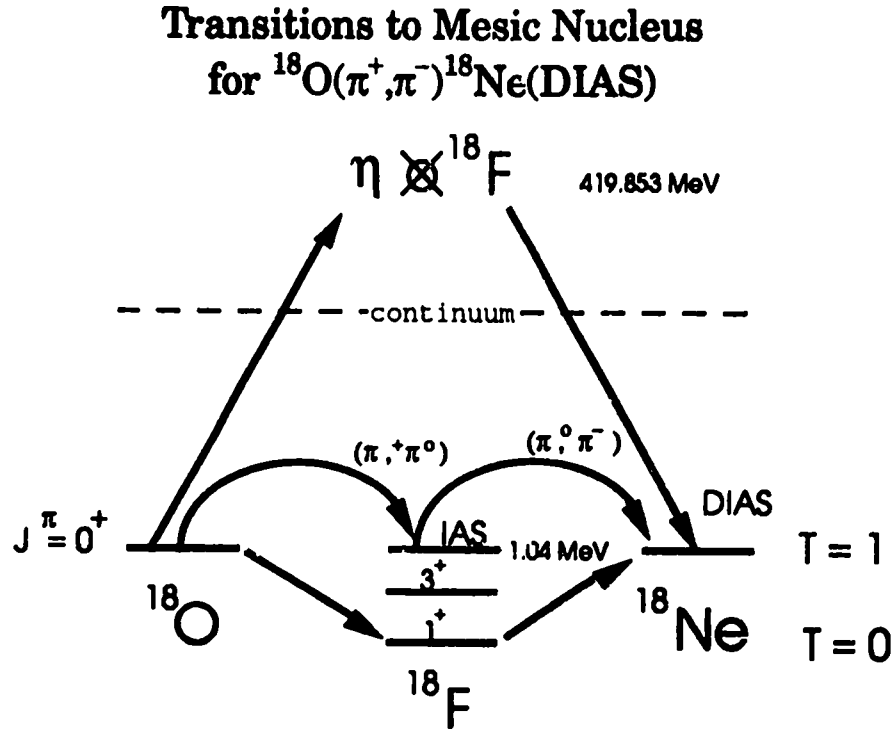
Figure 1.3: Transitions in the $^{18}O(\pi^+,\pi^-)^{18}Ne(DIAS)$ reaction to the intermediate bound state $\eta \otimes {}^{18}F$, and reaction mechanisms leading to the formation of a mesic nucleus [Ha-87].
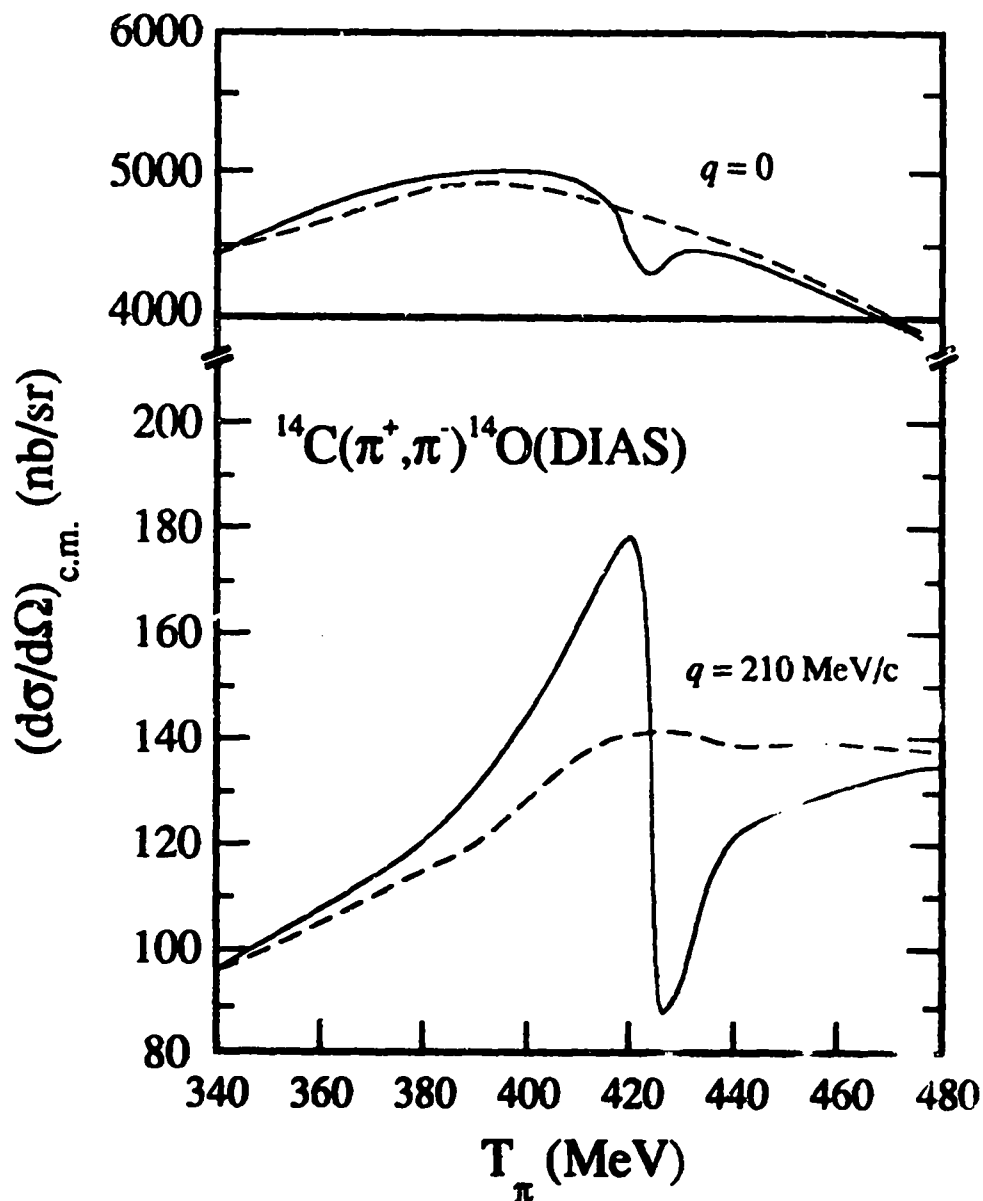
Figure 1.4: The calculated DCX excitation function for $^{14}C(\pi^+,\pi^-)^{14}O$ DIAS). The dashed and solid curves represent the non-resonant background and full calculation by Haider and Liu [Ha-87].
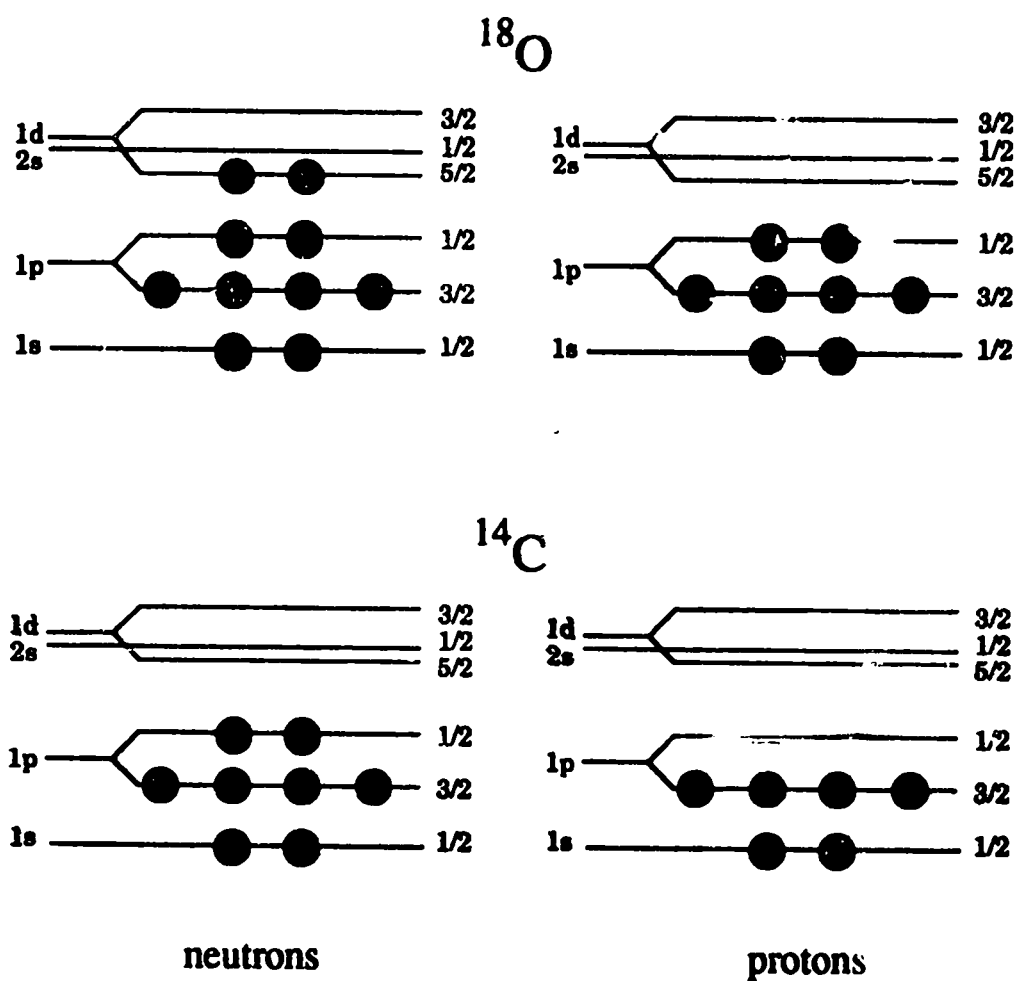
Figure 1.5: Shell model level diagrams for ^{14}C and ^{18}O.

the excitation function for the reaction $^{18}O(\pi^+,\pi^-)^{18}Ne$(DIAS). Measurements were made at momentum transfers of $q = 0$, 105 and 210 MeV/c over an energy range of $T_\pi =350$ to 440 MeV. The accelerator, spectrometer and the various hardware and software components of this experiment are discussed in Chapter 2. The data reduction is discussed in Chapter 3. The results and implications of experiment 1140 are presented in Chapter 4, and some theoretical considerations of the η bound state, the compound nucleus and resonance shapes are covered in Chapter 5.

Chapter 2

Experimental Set-up

2.1 The LAMPF Accelerator

The Clinton P. Anderson Meson Physics Facility (LAMPF) consists of a linear accelerator which feeds several experimental areas with H^+, $\vec{H}$ and H^- beams. Fig. 2.1 shows the layout of the LAMPF experimental areas.

The LAMPF accelerator [La-84] has two main sections, a 100 MeV drift tube linac and a side coupled linac which can accelerate the beam to 800 MeV. A 50 mA ion source along with a 750 keV Cockroft-Walton accelerator inject positive ions into the 201.25 MHz drift tube linac. The same thing is done with negative and polarized ions. The accelerator is then able to provide H^+, $\vec{H}$ and H^- to different experimental areas by chopping the beam into bunches with a typical length of 500 μs. Beam gates for the H^+ beamline have a typical macrostructure of 120 Hz. The accelerator provides a variable energy H^+ beam with currents delivered to area A of 100 to 1000 μA. Typical beam currents for experiment 1140 were about 500 μA.

Before the beam arrives at P^3 there are two targets that it goes through. The beam first passes through the Thin Target station (AT) for the Time of Flight Isochronous (TOFI) spectrometer, then it passes through the A1 target, the production target for the Energetic Pion Channel and Spectrometer (EPICS) and the Low-Energy Pion (LEP) channel. These targets

degrade the beam by $\sim$ 23% in intensity [La-84] before it reaches the A2 production target, which produces pions for the P^3 channel. The AT, A1 and A2 beamlines are shown in Fig. 2.2. The A2 production target is a graphite target 4 cm thick which provides pions with a maximum energy of 625 MeV to the P^3 experimental areas. The beam spot size is approximately 5 mm $\times$ 5 mm at the A2 target. After the A2 target there is a collimator, 3PCL1E1, which is used to reduce the horizontal width and improve the momentum resolution of the beam as it passes through the transport system to P^3. The A2 target collimator, 3PCL1E1, is controlled by the central control room and must be calibrated before it is used. A scan was made comparing the pion beam current with the proton beam current as the collimator was moved. In 1991 the collimator was set at 6.75 cm. Fig. 2.3 shows the results of the 1991 collimator scan. Because of the low beam current delivered to area A, and in order to maximize pion flux, 3PCL1E1 was not used during 1992. This reduced the momentum resolution somewhat for 1992 runs. Fig. 2.4 shows both the A2 target and the collimator jaws, 3PCL1E1 at the entrance to the P^3 channel.

2.2 The P^3 Channel

The High-Energy Pion Channel (P^3) uses the A2 graphite target to produce high intensity pions for delivery to one of two experimental areas. The P^3 transport channel can be set-up to deliver positive or negative pion beams to P^3–East or P^3–West. Fig. 2.5 shows the path that pions take after the A2 target. The P^3 channel has low background contamination moderate resolution and a well defined phase space [La-84]. In order to improve the energy resolution a dispersed beam tune was used. This tune delivered a beam
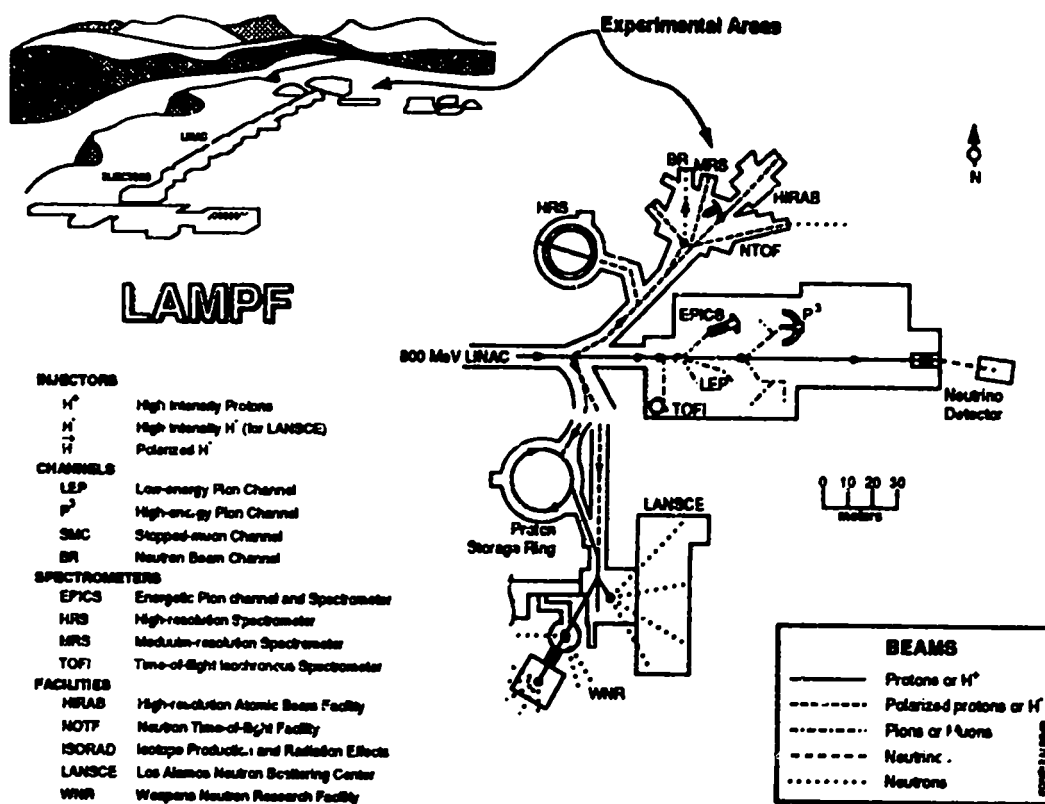
Figure 2.1: The Clinton P. Anderson Meson Physics Facility (LAMPF).
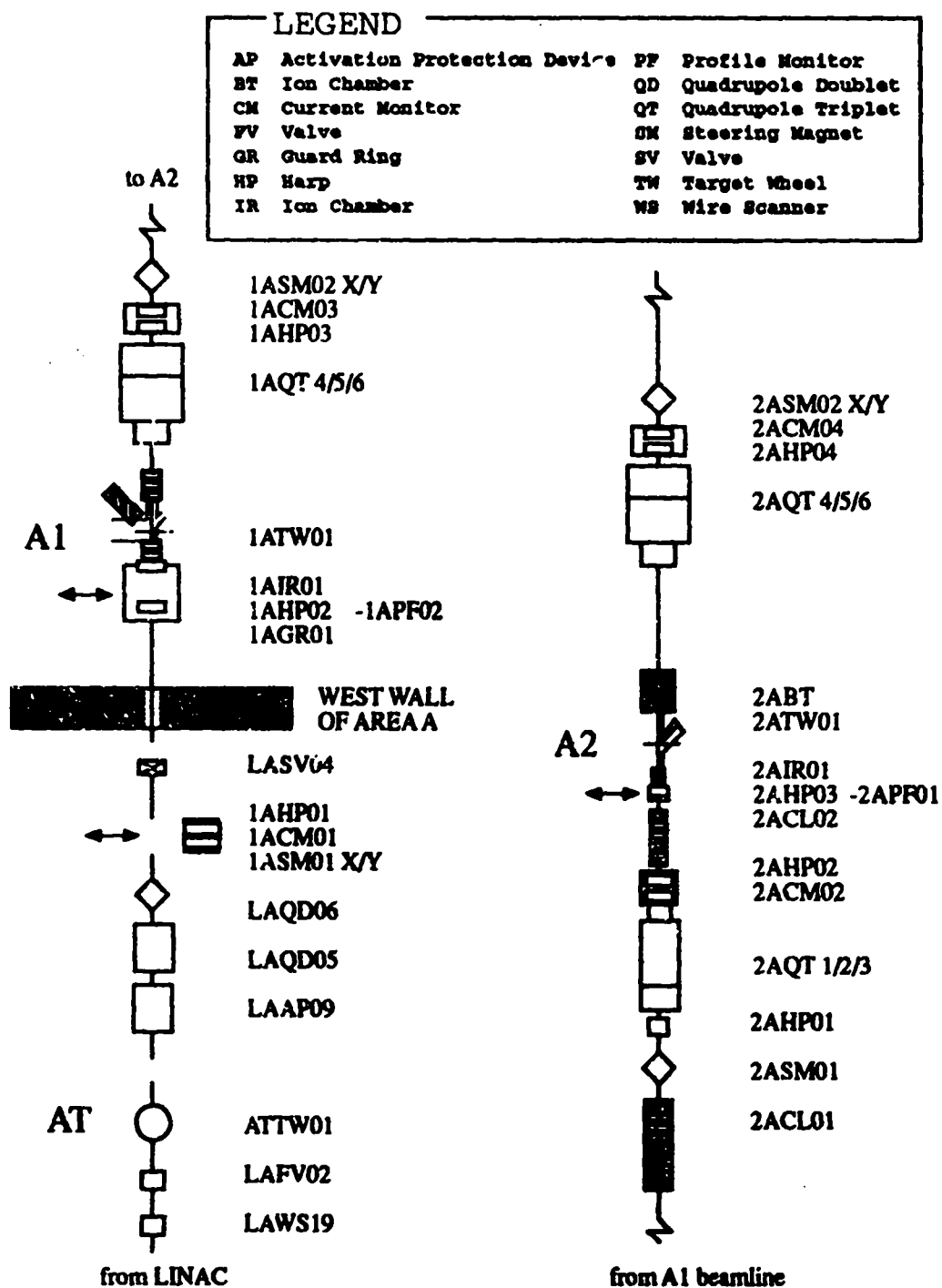
Figure 2.2: LAMPF beamline monitors and transport system for AT, A1 and A2 beamlines.
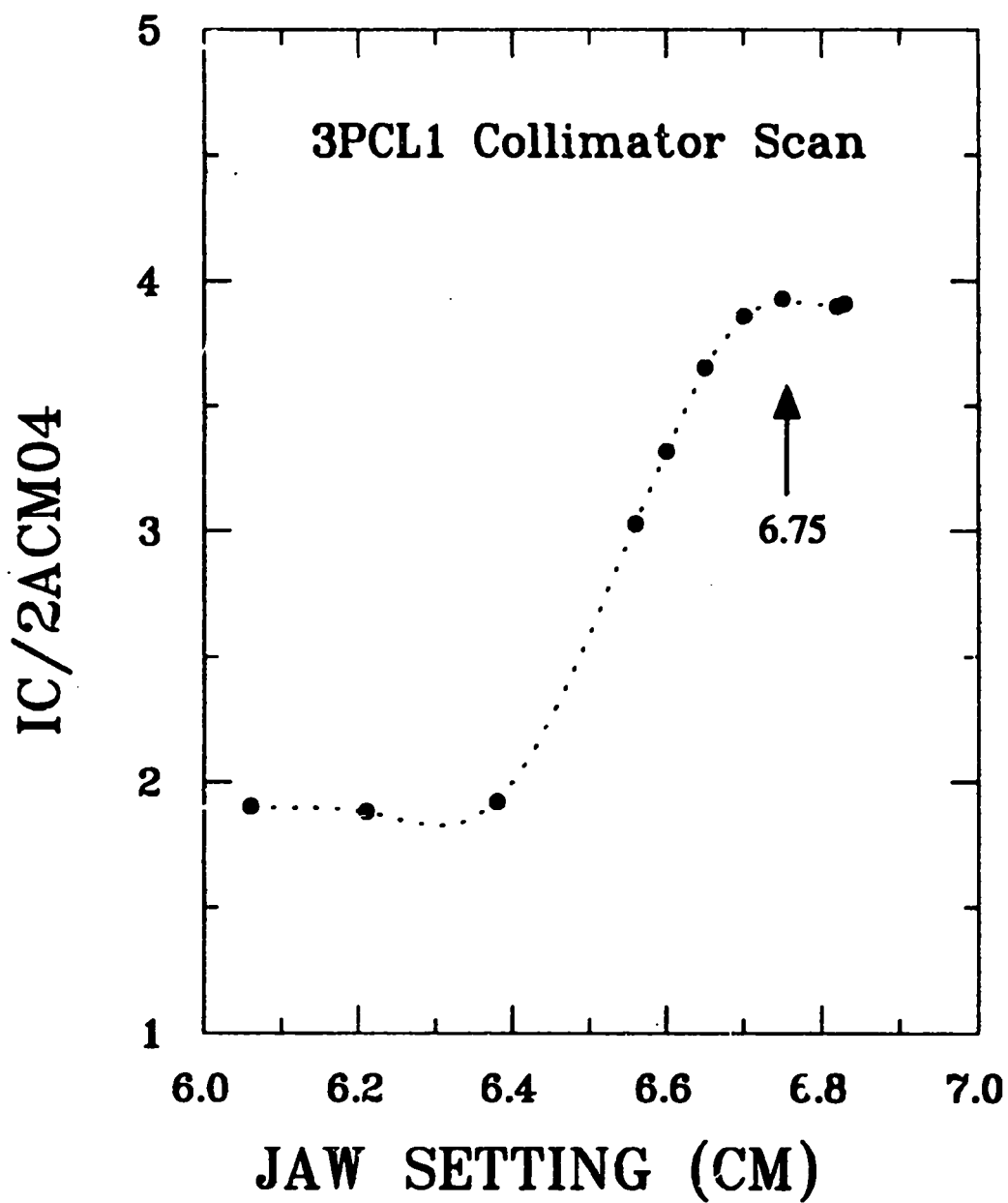
Figure 2.3: 3PCL1E1 collimator position scan (1991).
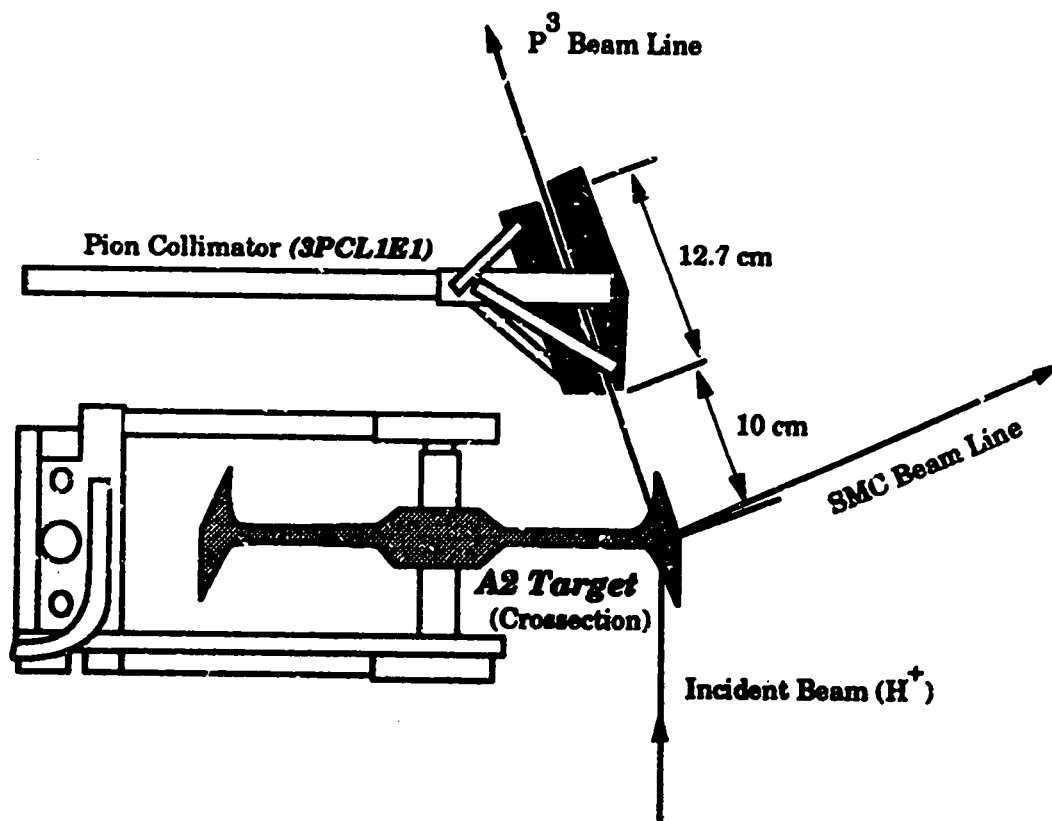
Figure 2.4: The 3PCL1E1 collimator and A2 target.

Table 2.1: P^3—East channel magnet control voltages for a dispersed beam tune of π^+ at 400 MeV.

Magnet	Control Voltage	Polarity
BM01	24620	Reverse
BM02	28064	Reverse
BM03	29499	Normal
QM01	23674	Reverse
QM02	17055	Reverse
QM03	15857	Normal
QM04	22968	Normal
QM05	16990	Reverse
QM06	20422	Reverse
QM07	32976	Reverse
QM08	31981	Reverse
QM13	3561	Reverse
QM14	14630	Reverse
QM15	9552	Normal
QM16	8171	Normal
QX01	26298	Reverse
QX02	46745	Normal

spot of about 2.5 cm(horizontal) × 3.5 cm(vertical) with an energy resolution of 0.15% to the LAS spectrometer. The channel magnets were set by the computer code MON90 [Mo-90], which determines the correct control voltages for BM02 and BM03 were varied to maximize the current in a thin ion chamber immediately upstream of the target chamber. Typical dispersed beam control voltages for incident π^+ at 400 MeV are listed in Table 2.1. In the P^3—East experimental area, the quadrupole doublet QX01 and QX02 provide final beam focusing, and vertical and horizontal steering are done with SMV and SMH. The pion flux incident on the target was approximately $1 - 2 \times 10^7$ π^+/s at $T_\pi = 400$ MeV.

P³ CHANNEL

Figure 2.5: The LAMPF P³ Channel.
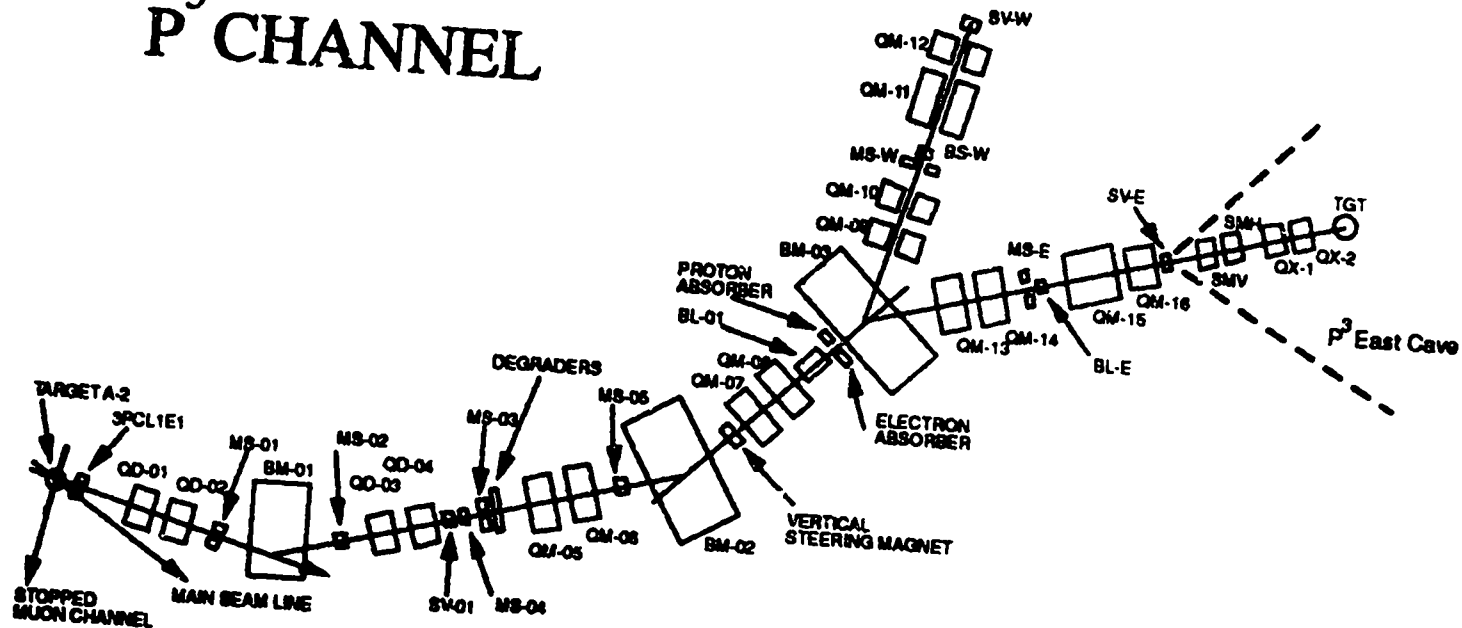
LEGEND

QD	QUAD MAGNET
MS	MOVEABLE JAWS
BM	BENDING MAGNET
BL	BEAM PLUG
SV	VACUUM VALVE
QM	QUAD MAGNET
QX	QUAD MAGNET-COUPLED
SM	STEERING MAGNET-DIPOLE

REF drawing by Esquibel, MP-7
APRIL 3, 1979, Revised JJ 8/25/91

A series of jaws are used to define the phase space of the channel. The features of these jaws is listed below [P3E-87].

MS01 Determines the horizontal angles of the beam after the A2 target. Along with MS02, it defines the solid angle of the beam after A2. MS01 defines the depth of focus in the dispersion direction at the scattering target.

MS02 Determines the vertical angles of the beam after the A2 target. Provides medium resolution with YTGT cut.

MS03E This jaw provides a slight momentum cut along with MS03W, but it mostly reduces spills at QM07.

MS03W This jaw provides a slight momentum cut along with MS03E, but it mostly reduces spills at QM07.

MS04 These are vertical collimator jaws positioned near the momentum jaw, used to reduce vertical beam spot size.

MS05 These are another set of vertical jaws upstream of BM02. They help set the beam intensity, and have little correlation with vertical beam spot size.

2.3 The Large Acceptance Spectrometer

The Argonne Large Acceptance Spectrometer (LAS) is a 45 degree dipole, which has been modified to include a C-magnet, a quadrupole doublet (QL01 and QL02), two pairs of drift chambers (used for particle tracking), a Cherenkov detector (used to reject electron events), and two scintillators

(used to determine time-of-flight for particle identification). Fig. 2.6 shows a schematic of the spectrometer in its full configuration. The LAS dipole has a 45° bend, a momentum bite of ± 10%, and subtends a maximum solid angle of ~12 msr [Od-91]. The C-magnet was used to sweep away protons and positive pions and gave a 10° horizontal bend to particles with the correct momentum. The general properties of the spectrometer is given in Table 2.2. The LAS dipole and the quadrupole doublet are also set using the computer code MON90 in a similar manner to the channel magnets. The C-magnet shunt voltage is set by hand, scaling Eqn. 2.1 to put it in the correct units. Typical spectrometer magnet settings for π^- at $T_\pi = 400$ MeV are listed in Table 2.3. All of the magnets were set up for $\delta = 5\%$. The central momentum of the spectrometer can be written,

$$p_o = \frac{p_c}{(1 + (\delta/100))} \tag{2.1}$$

where p_c is the momentum of the outgoing π^-. By looking at the acceptance of the spectrometer, a median value δ was chosen. As shown in Fig. 2.7, $\delta = 5\%$ is near the center of the spectrometer acceptance and will allow the greatest range of magnet settings without having to correct for the acceptance of an individual run.

Helium bags, installed beginning after the target chamber and continuing through to the rear chamber, were used to minimize multiple scattering.

2.4 Detectors and Electronics

There was one pair of delay-line readout drift chambers before and one pair after the dipole used for particle tracking. These chambers were numbered

Table 2.2: Properties of the Argonne Large Acceptance
Spectrometer [Od-91].

	with C-magnet	without C-magnet
Solid Angle (msr)	12	15
Flight Path (m)	7	6
Momentum Bite (%)	±10	±10
Horizontal Angular Acceptance (deg)	+4.5 -2.3	±3
Horizontal Angular Resolution (deg)	0.25	C ˆ5
Vertical Angular Acceptance (deg)	±2.5	±4
Vertical Angular Resolution (deg)	0.5	0.5
Vertical Target Position Resolution (mm)	3	3
Horizontal Target Position Resolution (mm)	1.5	1.5

Table 2.3: P^3—East spectrometer control voltages for π^- at 400 MeV. The C-magnet shunt is listed in volts, all the other spectrometer magnets are listed in terms of DAC units.

Magnet	Control Voltage	Polarity
C-magnet	48.22(V)	Reverse
QL01	16474	Reverse
QL02	34781	Normal
LAS	41385	Reverse

Large Acceptance Spectrometer (LAS)
(with Cherenkov detector)

CHERENKOV DETECTOR

DIPOLE BENDING MAGNET

MWDC #6

MWDC #5

S3

S2

HERMES C MAGNET

2 COUPLED QUAD MAGNETS

MWDC #1

ALAS

TARGET

BEAM

Q1

Q2

TERI

ARLENE

MWDC #2

AIR PAD CONTROL SYSTEM

PIVOT

AUTOMATIC LEVELING SYSTEM

AIR PADS
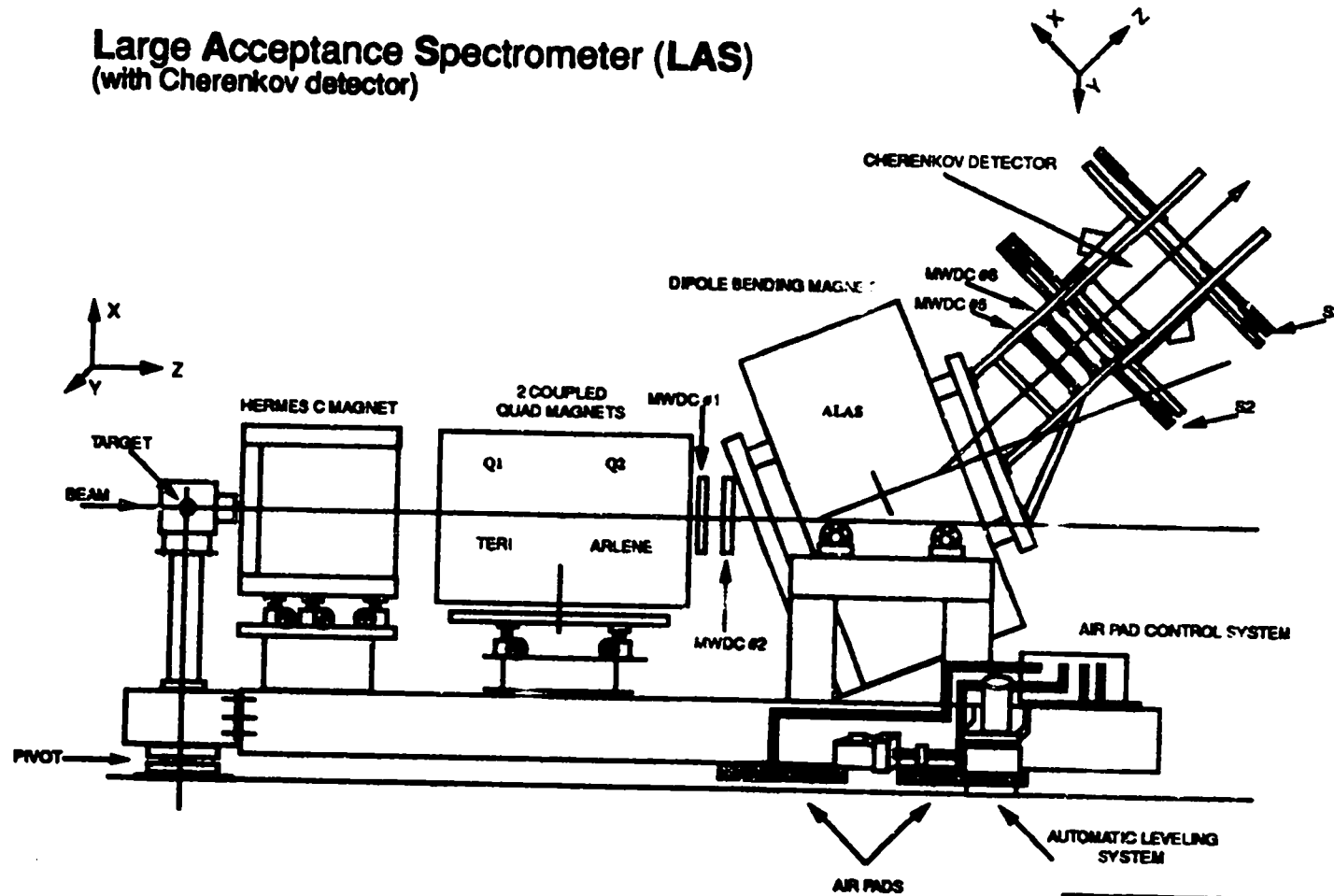
REF 60Y-181545, 60Y-181542
modified by JJ
JULY 25, 1991

21
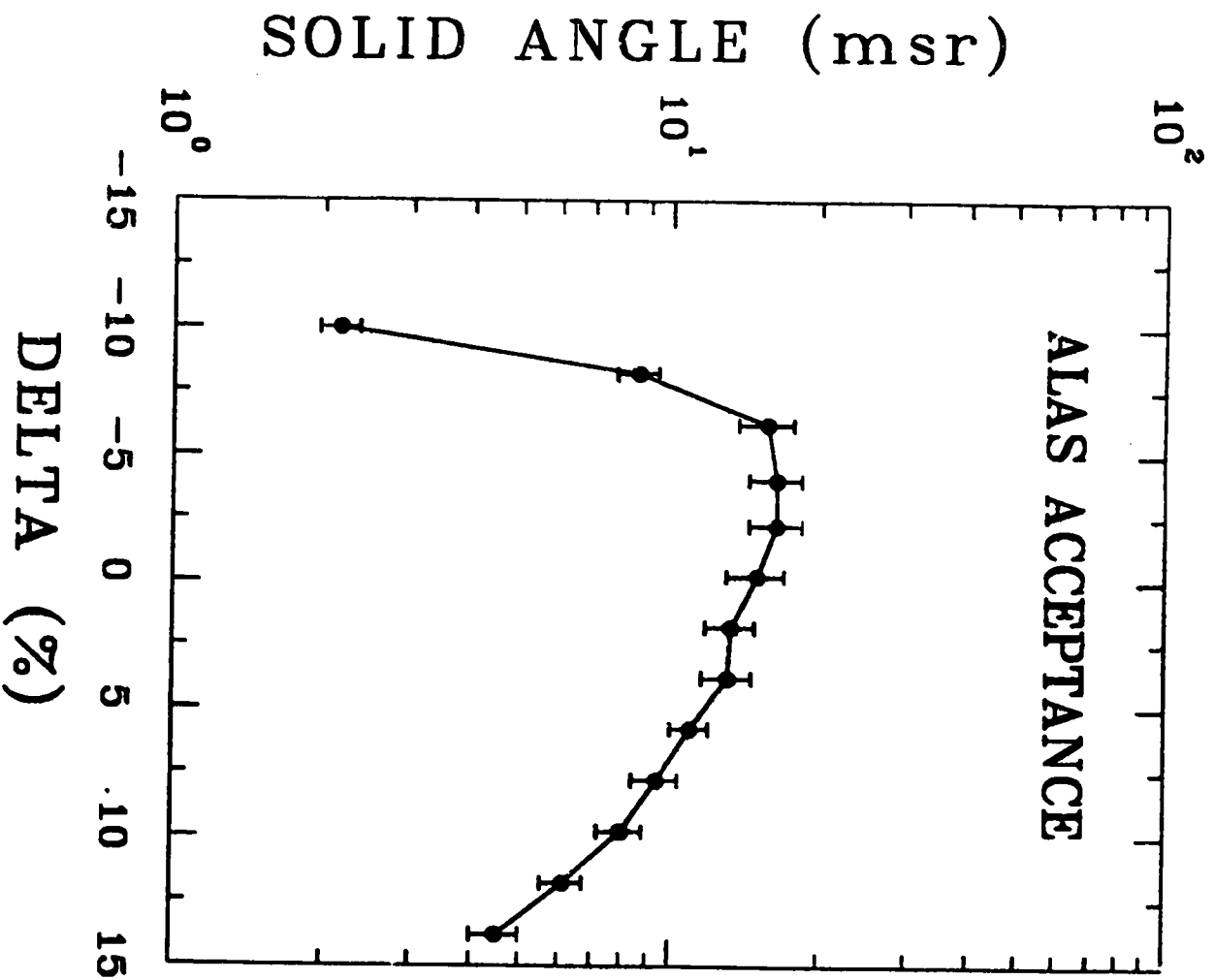
Figure 2.7: Acceptance of the Large Acceptance Spectrometer (LAS) [W91].

1, 2, 5, 6 respectively. For a given event, the chambers provide particle positions which are traced back to the scattering target. This information is combined with the time-of-flight information from the scintillators to identify the reaction. A *good event* is defined as a coincidence between the two scintillators and one front chamber. The wire chambers and scintillators (photomultiplier tubes) were individually plateaued, using beam particles, to find their optimal operating regions. The wire chambers were maintained at 2050 V and the scintillators S2N, S2P, S3N, and S3P were set at 1805, 1800, 1650, and 1725 V respectively. The chambers used the mixture of gases, 65% argon, 35% isobutane and 0.5% isopropyl alcohol, which was kept at a slow flow rate, keeping the chambers at approximately 1 atmosphere of pressure [At-81, Mo-78].

A gas threshold Cherenkov detector containing isobutane was used to eliminate electron events. The Cherenkov detector has been found to be $\sim$ 99.7% effective [Wi-91]. The Cherenkov detector was operated at 2300 V.

Signals from the wire chambers are converted to digital signals using analog-to-digital converters (ADC) and time-to-digital converters (TDC) and are then transmitted to the CAMAC controller in the counting house using cables. Various logic modules, scaler modules and the LAMPF gate generator (LGG) are used in the experiment electronics. Figs. 2.8-2.10 show the electronics set-up for this experiment. These signals are sent to the counting house MicroVax computer where some events are analyzed on-line, and all of the raw event signals are written to magnetic tape for replay off-line. The CAMAC system [Cl-82] exchanges data with the computer via a Micro Branch Driver (MBD) [Sh-74]. The LGG generates a RUN gate. Beam gate (BG) signals corresponding to the macrostructure of the accelerator and the RUN gate are

used so that scalers accumulate only when a beam pulse is delivered to the experimental area. By using the LGG in conjunction with the ion chamber, data is accumulated only when a current is registered in the ion chamber.

The LAS dipole current is monitored by a digital multi-meter. In order to accurately monitor the LAS dipole magnetic field, an NMR probe was attached to the dipole pole face where it would not interfere with particle transport.

2.5 Thin Ion Chamber

The incident pion flux was monitored by a thin ion chamber immediately upstream of the target chamber. This ion chamber was used for beam normalization. The chamber, shown in Fig. 2.11, used an aluminum container with about an 8.5 inch × 2.25 inch window. The windows were made from 1/4 mil aluminized mylar. The chamber contained two DC high voltage planes, which were kept at 100 Volts, and a central signal plane, all composed of 1/4 mil aluminized mylar. The gas mixture used was 80% argon, 20% CO_2 and the chamber was operated at 1 atmosphere of pressure. The chamber was plateaued after completion of the experiment, the results are shown in Figure 2.12.

The ion chamber was used in normalizing runs by collecting ions on the central signal plane. At high beam currents, it is possible that the ion chamber would become saturated, or unable to refresh itself fast enough to accurately monitor the beam flux. The beamline jaw MS01 and the incident pion energy were varied and the results are shown in Figures 2.13 and 2.14. Fig. 2.13 graphs the yield given by the ion chamber against the scaler ratio
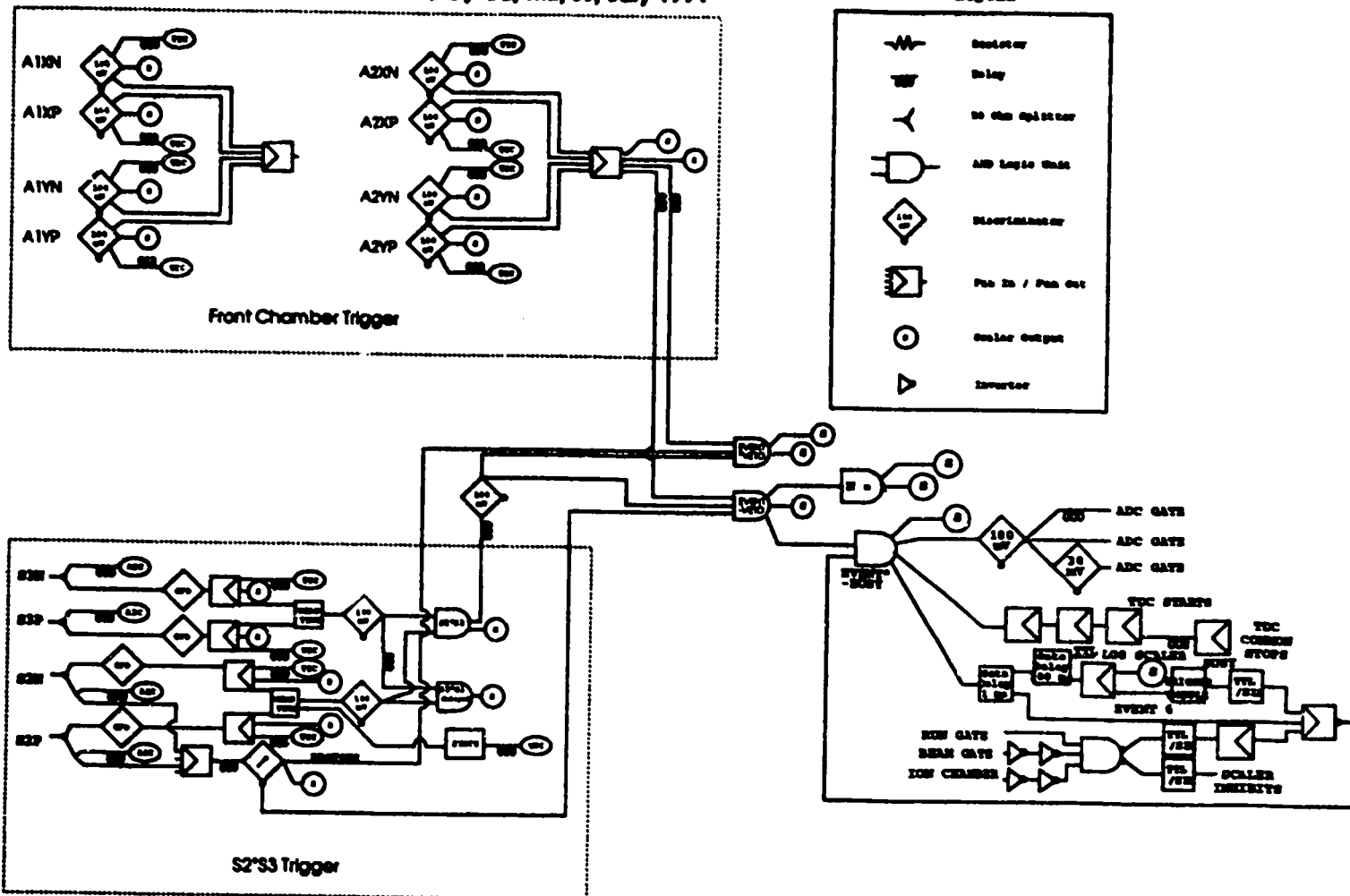
Figure 2.8: Front chamber and trigger electronics for E1140.

Figure 2.9: Rear chamber and Cherenkov electronics for E1140.
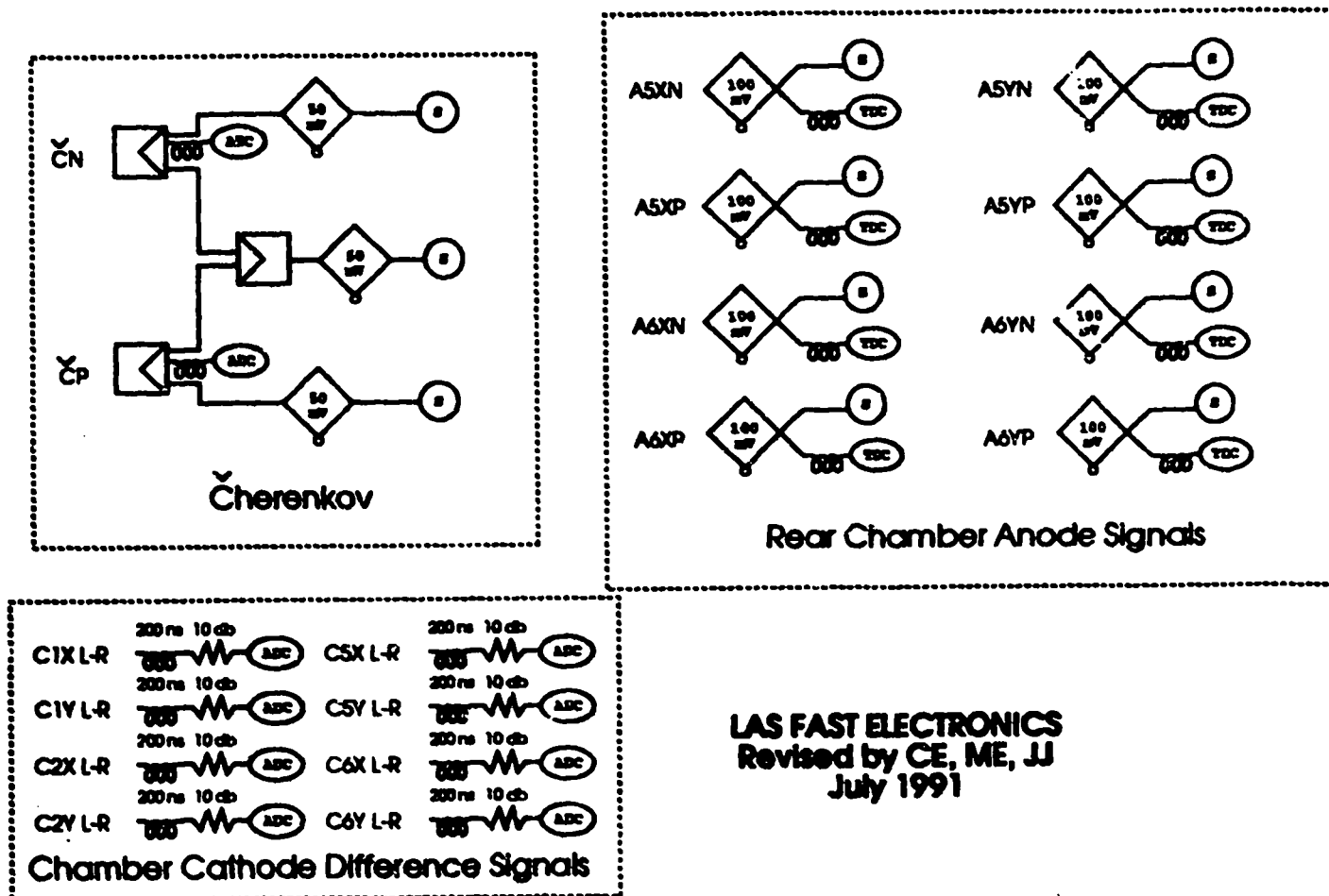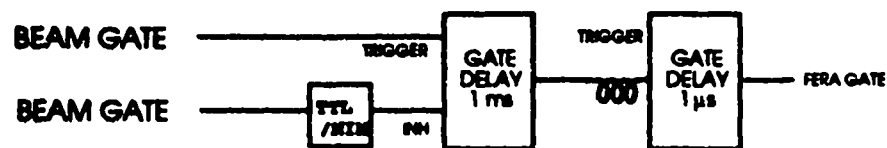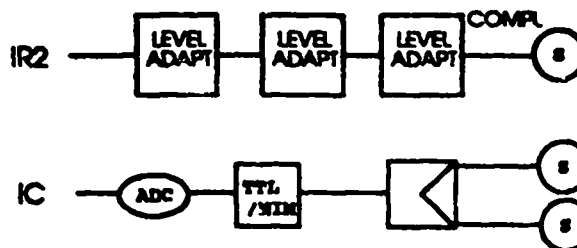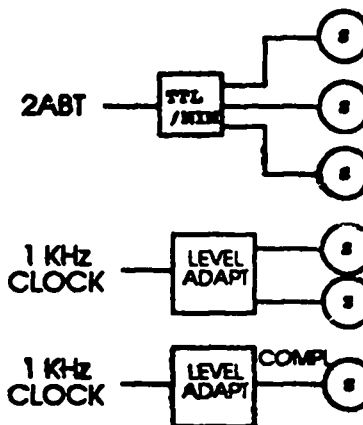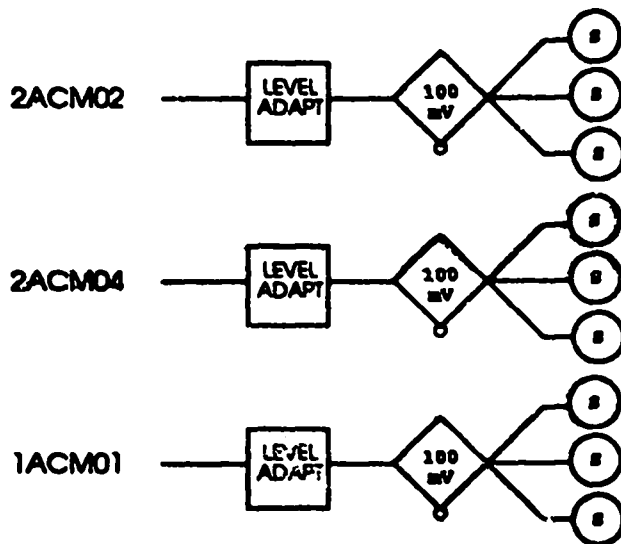
Figure 2.10: Various scaler electronics for E1140.

Front View

Side View (cutaway)

-HV

signal plane

-HV

Top View

Gas Out   High Voltage

Signal   Gas Out
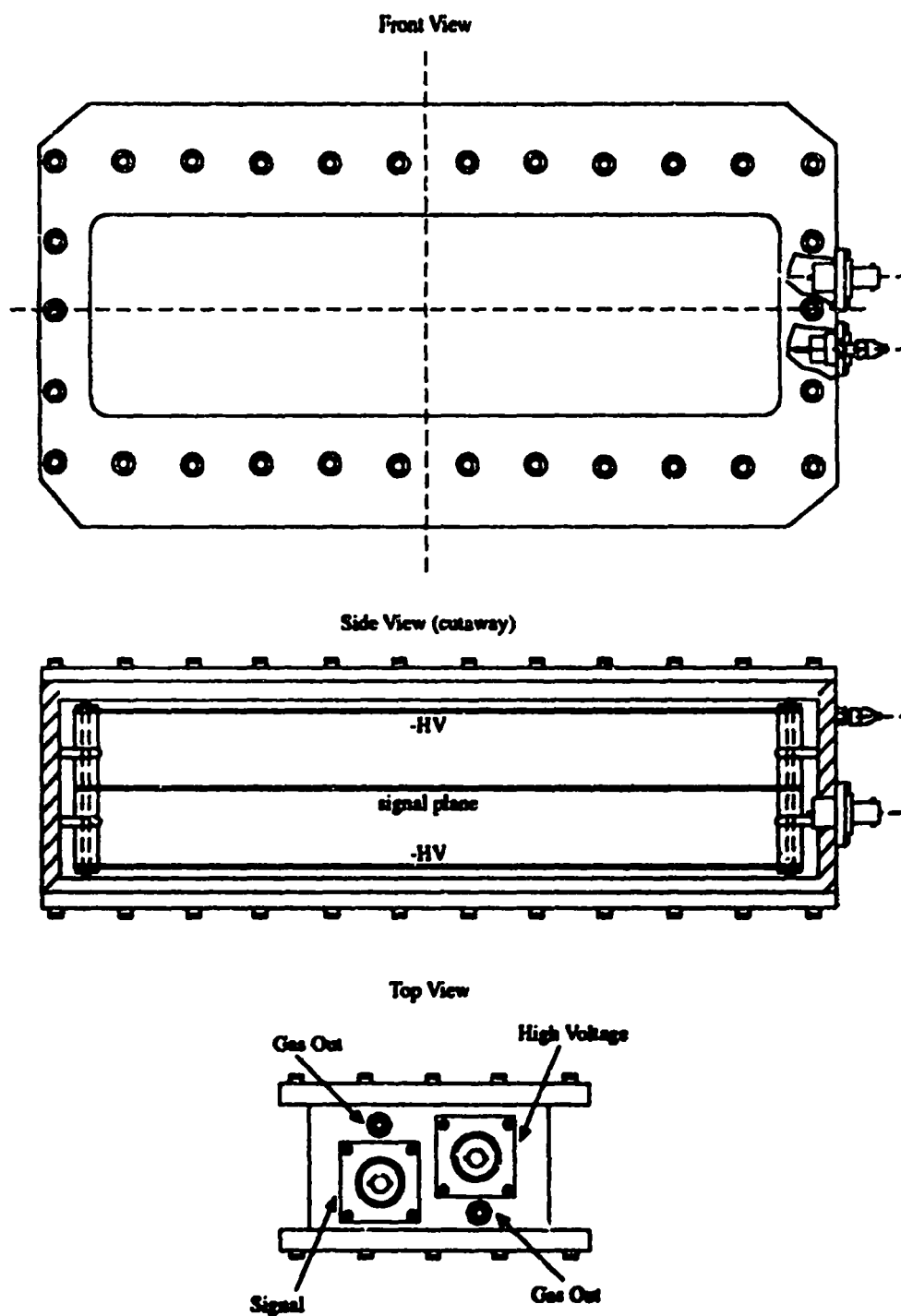
Figure 2.11: A schematic view of the thin ion chamber.
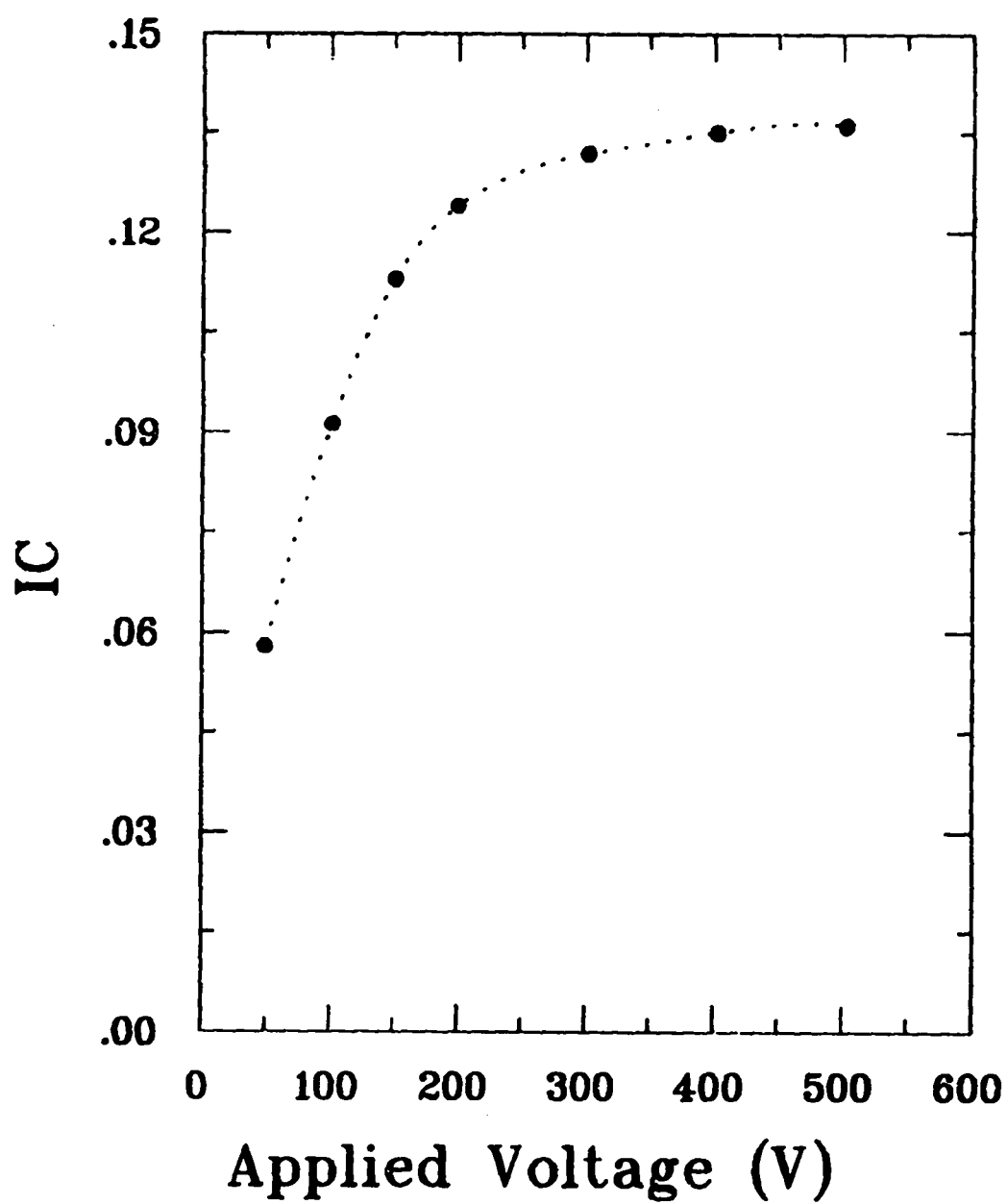
Figure 2.12: Plateau of the thin ion chamber.

IC/hour for incident pion energies of $T_\pi = 390, 400, 420$ MeV. The fits to the data are to help guide the eye and indicate that that a linear relation exists between these two variables. It is also shown that as the energy increases the yield decreases. Fig. 2.14 plots the MS01 slit opening against yield at 420 MeV and also gives a linear relationship. Since neither of these plots shows a drop off corresponding to chamber saturation, the ion chamber should be a consistent beam monitor and provide a robust means of beam normalization.

2.6 Targets and Scattering Chamber

The DCX target used was liquid H_2O with an isotopic purity for ^{18}O of 94%. The active area of the target measured 6.66 cm (horizontal)$\times$ 7.56 cm (vertical) and the target windows were made of CH_2,0.159 cm thick. The target had a width of 1.50 cm which bulged slightly in the center. By using both CH_2 and ^{18}O targets with hydrogen kinematics, it was possible to cross-normalize and experimentally determine the areal density for this target. The ^{18}O target areal density was measured to be 1.62 g/cm^2. To correct for the isotopic purity, divide through by the isotopic purity of 94%, to get the effective areal density of 1.72 g/cm^2. The CH_2 areal density was measured to be 0.294 and 0.288 g/cm^2 for 1991 and 1992 respectively. The beam was found to fully intersect all of these targets.

The scattering chamber was filled with helium at atmospheric pressure for both DCX runs, with the ^{18}O target, and CH_2 normalization runs. To minimize multiple scattering and energy loss in the target, it was determined that the target should be kept at half of the scattering angle. Therefore, when
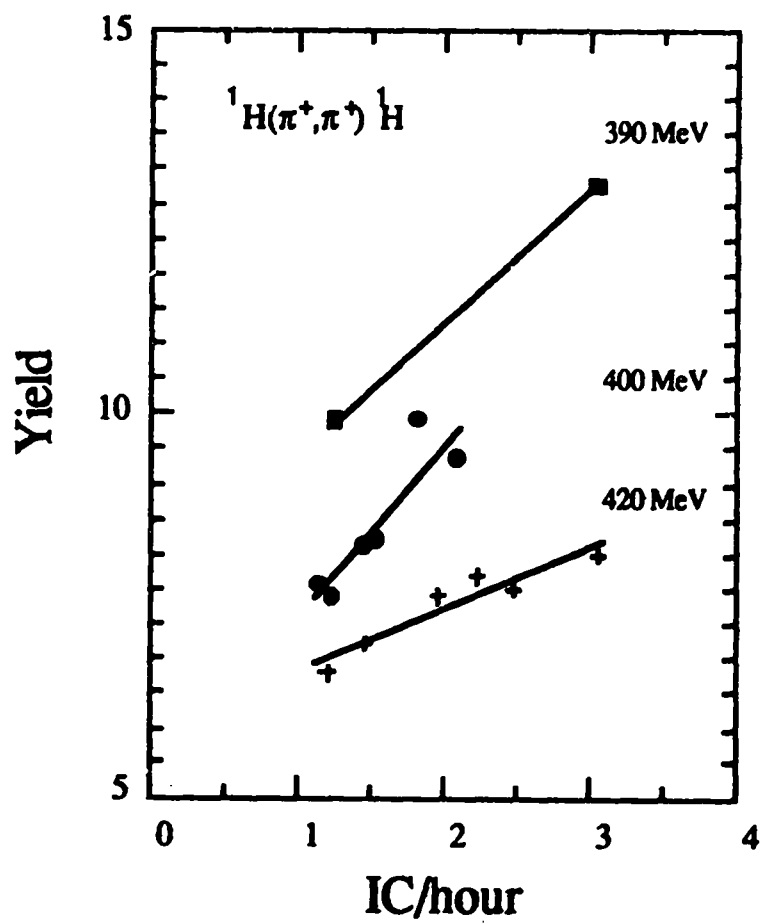
Figure 2.13: Yield as a function of IC/hour at $T_\pi = 390, 400, 420$ MeV.
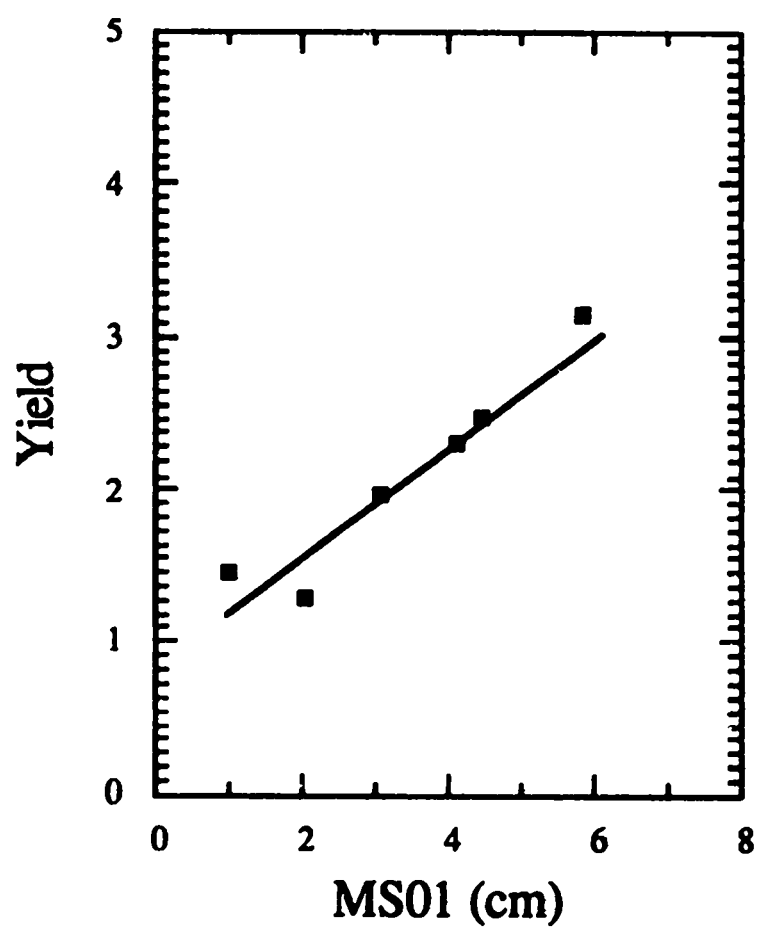
Figure 2.14: Yield as a function of MS01.

the spectrometer was set to a floor angle, θ_{floor}, this corresponded to a scattering angle of $\theta_{scat} = \theta_{floor} - 10°$, subtracting off the 10° bend of the C-magnet. The scattering chamber would then be set to $\theta_{scat}/2$.

2.7 Software

The data acquisition software used used to acquire and analyze data for this experiment was the Q software package. This discussion is intended to familiarize the reader with the Q package, especially in relation to this experiment. Some basic Q commands are listed in Table 2.4. For a more in depth discussion of the Q package refer to the "Q System – Programmer's Information Manual" [Q-89].

The most important part of the data acquisition software is the analyzer, QLAS87.EXE. This program coordinates the acquisition of data from CAMAC via the MBD. It also processes *good events* and writes them to tape. When the data is taken, only a fraction of the events may actually be analyzed, since writing the events to tape takes precedence. During replay of the data, the analyzer will process every event. CAMAC delivers these events as data words to the analyzer. The file BLK001.TXT is used to tell the analyzer the location of each data word in terms of crate, slot and input location. When the analyzer is initialized, by an @QSTART command, the computer looks at the file CANS.COM to define the location and name of the analyzer, the events to analyze and whether the mode is data acquisition or replay. The QANS.COM file used for data acquisition is shown in Table 2.5.

One feature of the analyzer is that it will call a kinematics subrou-

tine, CALKIN, to determine particle momentum, missing mass and scattering angle. Together with polynomials that have been written to describe particle trajectory through the spectrometer, it is possible to trace the particle back to the scattering target. This allows the experimenter to extract a large number of variables from the given scaler inputs. These variables include information in x, y, θ, and ϕ which are used with relative time-of-flight information and summed pulse heights for various calculations. These calculated quantities, along with some parameters input by the experimenter, are stored in the dynamic parameter array (PRM) database. The various scalers can be listed with SLR.

Some scaler events have already gone through hardware cuts, for example, the proton veto, in hardware, rejects proton events by setting the discriminator level to reject events with pulse heights above a certain level. This is done because protons deposit more energy than pions and have correspondingly larger pulse heights. Most of the cuts and tests, however, are made with the software. This allows the most flexibility for analyzing the data. The experimenter uses the Q test package to eliminate undesirable events, such as muons, electrons and cosmic rays. Most tests are defined with the program TSU. When the Q analyzer is initialized this program is run and it sets up the tests which are defined in an experiment specific file. This experiment used the file E1140.TST, a portion of which is shown in Table 2.6, to set gates and to make logical tests on the data. Indirect gates may be set up interactively in the histogramming package HPL. In HPL it is possible to view the data in terms of histograms and then set gates, or boxes. The indirect gates and boxes are then saved in the file TSTDAT.DAT. Fig. 2.15 shows an indirect

box around the data corresponding to particles that may be from the correct reaction. This box specifically excludes protons, but is likely to include some muons and electrons. These particles can be eliminated using other software tests. The geometric mean of S2 and S3 pulse heights is plotted along the x-axis and the time-of-flight from S2 to S3 is plotted along the y-axis. It is easy, using this type of a histogram, to set up a test which excludes events that survive the less stringent hardware cuts.

The histogramming package, HPL, is the graphical interface for Q. HPL not only allows the user to place indirect gates or boxes on the data interactively, but it also allows the user to check that various experimental components are calibrated properly. For example, it is possible to look at the pulse heights and time signals to determine if chambers are calibrated. HPL also allows the user to observe raw and analyzed events as they are processed by the analyzer. Some basic HPL commands are listed in Table 2.7. The histograms used by HPL are set up in HSU from the file E1140.HST when the analyzer is initialized. An example of part of this file is given in Table 2.8.

2.8 Experimental Set-up and Calibrations

Before data is taken, it is necessary to calibrate and test the various experimental equipment, to set-up the electronics, and to set-up the experiment specific software. First, the Q software package discussed in the previous section is installed and the detectors and other equipment are set-up. Next, high voltage cables and signal cables are connected between the experimental area and the counting house. Gas is flowed through the various chambers for

about a day and high voltage is applied. If the chambers are able to maintain typical operating voltages for a day, anode and cathode signals are looked at with the HPL histogramming package, or by oscilloscope. At this point, the experimenter knows that the hardware is essentially set-up and proceeds to calibrate it.

For this experiment, the first calibration was to determine the delay necessary so that the two scintillators, S2 and S3, would fire in coincidence when a pion passed through. This was very important, since the trigger event would be a coincidence in both scintillators and one of the front chambers. The first scintillator, S2, would then define the start times for the TDC channels. Each wire chamber consists of alternating anode and cathode wire planes. The anode wires are kept at high voltage and there is a TDC converter at each end of an anode delay line, as shown in Fig 2.16. In order to remove the ambiguity as to whether a particle passed on the left or right of the anode, the cathode wires are alternatively bussed as left or right signals and the difference of these two signals is sent to an ADC converter. By having an associated positive or negative pulse with each TDC signal, it is possible to determine the particle position without this left-right ambiguity. Indirect gates are set around the left and right signals for each plane, using HPL. Correlations between pairs of wire planes, such as X1 and X2, can be removed by varying certain parameters in the dynamic parameter array (PRM) and observing the effects in the dotplotting routine HDO.

The TDC signals from each end of the anode delay line are subtracted,

and the difference, t_d, can be used to determine the particle position, x.

$$t_d = t_1 - t_2 x = a_o + a_1 t_d + a_2 t_d^2 + a_3 t_d^3 \qquad (2.2)$$

Drift time histograms are accumulated and the code DRT is run to calibrate the drift characteristics of each wire plane.

Target calibrations in x, y, ϕ and θ, and other calibrations, such as, PHICHK, THTCHK and DELTA are made. In each case, rays are written to tape, using the program FPO. These rays are then used by the program RAY to optimize the polynomials that are used for tracking particles through the spectrometer.

2.9 Run Procedures

For every run where the scattering angle changed, the spectrometer was raised on air pads and moved to a floor angle $10°$ greater than the scattering angle, because of the $-10°$ bend added by the C-magnet. The spectrometer was then leveled with motorized legs. The scattering angle for hydrogen normalization runs was always $40°$ in order to reduce background events and to operate at an angle where the hydrogen cross section was strong and constant. For a fixed momentum transfer, the following formula was used to determine the correct scattering angle,

$$q = 2p_{channel} \sin \theta/2 \qquad (2.3)$$

where $p_{channel}$ was the incident pion momentum. After moving the spectrometer, the target ladder was set to the correct target, and the target chamber was rotated to half of the scattering angle.

It was necessary to determine the kinematics for each energy and target. The program KINREL [Kin] was used to do this. For the DCX runs, the kinematics for $q = 210$ MeV/c were used for all angles. This was possible because the spectrometer was set at a δ value of 5% and the momentum change between the lab angles of 5° and $\sim$ 22° was small. This was also done to save time by not having to cycle magnets between every run. Appendix A lists the ^{1}H and ^{18}O kinematics used for this experiment.

The magnet and jaws were set using MON90 and MAG [Mag], and then verified before each run. The magnets were set following their hysteresis curve, so that the field settings were consistent each time a certain shunt voltage was applied.

A current digitizer was used to read the ion chamber current. The current digitizer was set to the scale appropriate for each measurement. This was necessary since the flux changed with energy. Because the digitizer scale affects the accumulated scaler, IC, it cannot be changed during a run A digital voltmeter (DVM) was used to measure the shunt voltage on the LAS dipole. During the runs taken in 1991, the DVM was only accurate to two decimal places. Therefore, during the second half of the experiment in 1991, and for all of the 1992 runs, an NMR probe was attached to the interior of the LAS dipole, providing an accurate measurement of its magnetic field.

A personnel safety sweep (PSS) was performed before the experimental area could receive beam. This was to ensure that no one was left in the experimental area. With all the safety interlocks made, the beam plugs could be taken out. It was necessary to closely monitor chamber currents, especially

at forward scattering angles, so that the chambers were not damaged. Once this was done, a run was started.

.

Table 2.4: Basic Q commands.

Q Command	Definition
@QSTART	command file to initialize the Q system
@QSTOP	command file to shut down the Q system
QCM	logs comment to console and tape (if enabled)
QCOPY	copies a Q tape to/from a disk file
QCT	closes out a tape
QDT	disables output taping
QEN	enables/disable events in trigger module
QET	re-enables output taping after QDT command
QFI	finishes a run
QKI	kills the Q system
QNAMCR	create a Qname
QNAMDE	delete a Qname
QNAMLI	list defined Qnames
QNT	starts a new tape
QPA	changes analyzer processing status of events
QRE	resumes a suspended run
QRU	to start a run format: QRU run#,comments
QST	reports Q system status information
QSU	suspends a run
QTR	triggers an event in the trigger module

Table 2.5: QANS.COM

```
$QNAME :== E1140
$MYANL :== [MP10REP.EXP1140.ANALYZER]QLAS87
$MYHST :== 250000
$MYDIR :== SY:
$HFNAM :== E1140.HST
$TFNAM :== E1140.TST
$MODE  :== DATA ACQUISITION
$TPFMT :== 11M
$BDO   :== QLAS87
$TRIGC :== 2
$TRIGN :== 21
$MBDBU :== 1500
$MYEVT :== 6,8,9
$MYPRO :== 6,?8
```

Table 2.6: Selected portions of E1140.TST test file.

```
;P3-East   -- Large Acceptance Spectrometer High energy DCX
;
/TE:150/BL:3/IG:22/IB:10
;
BLOCK,1
;
; PID (Particle ID) box
;
19,IBOX,1,                        ;19      ;BOX 1 ==> PID
24,IOR,1,-1,                      ;24      ;LOOP1 COUNTER
;
;
BLOCK,2,
;
33,AND,25,26,                     ;33      ;front x's OK
34,AND,29,30,                     ;34      ;front y's OK
35,AND,27,28,                     ;35      ; rear x's OK
36,AND,31,32,                     ;36      ; rear y's OK
;
37,AND,33,34,                     ;37      ;all front OK
38,AND,35,36,                     ;38      ;all  rear OK
;
;TARGET TESTS
65,GAT,233,-500,500,              ;65      ;XTGT
66,GAT,234,-1500,1500,            ;66      ;THTTGT
67,GAT,235,-800,200,              ;67      ;YTGT
68,GAT,236,-1500,1500,   ;68      ;PHITGT
;
;GATES AND BOXES
;
79,IBOX,6,                        ;79      ;BOX 6
80,IBOX,7,                        ;80      ;BOX 7
;
81,IGATE,1,                       ;81      ;IGATE 1 CHERENKOV PI's
84,IGATE,4,                       ;84      ;IGATE 4 Elastic Peak
86,IGATE,6,                       ;86      ;IGATE 6 El. Missing Mass
```
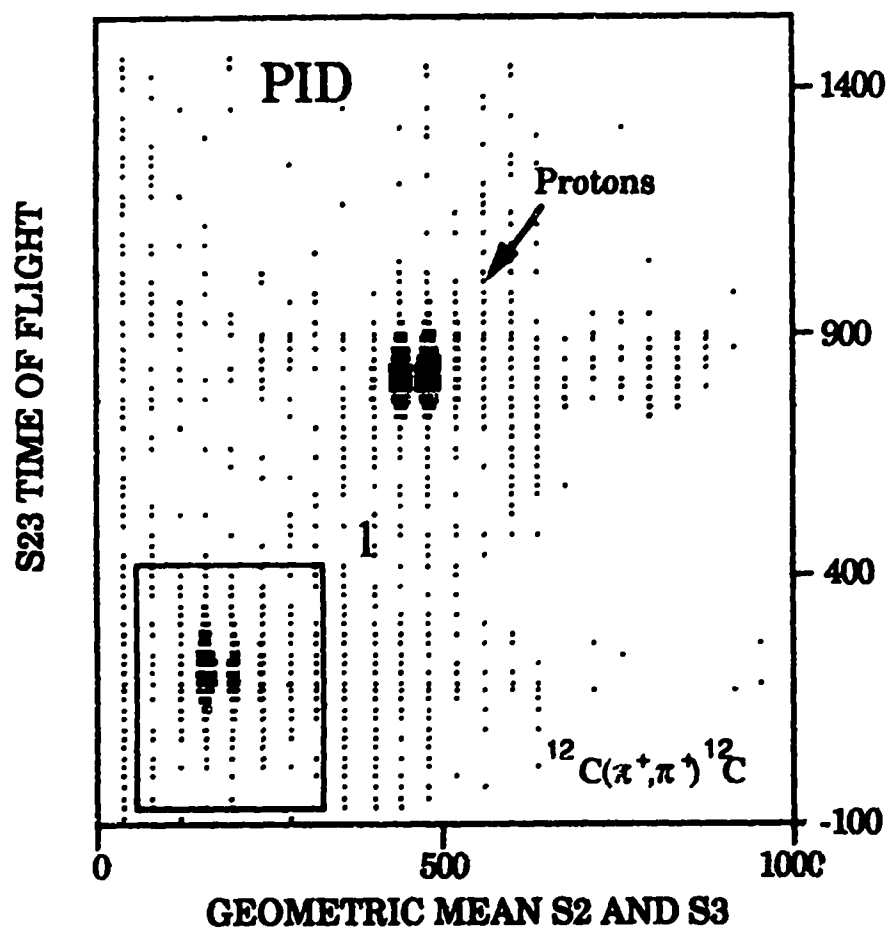
Figure 2.15: Particle identification histogram (PID) for $^{12}C(\pi^+,\pi^+)^{12}C$ at 400 MeV. The indirect box, labeled 1, excludes protons and some non-pion events.

Table 2.7: Basic HPL commands.

HPL Command	Definition
/AU	carriage return same as /SH
/BO:#m:xmin:xmax:ymin:ymax	to set marker box
/CL[:n][:all]	clear histograms
/DE[:n][:all]	delete histograms
/EX	examine display parameters
/FI:tsk	fit data with program tsk
/HC	make hardcopy of screen on laser printer
/LI	list histogram parameters
/MA	list set up markers (1-P hist only)
/MA:x1:x2:....:x10	put markers at x=x1,x2,...x10
/M.\:#m:x	put marker m at x
/MA:CU	set up markers with cursor
/-MA:m1:m2:....:m10	delete markers m1,m2,...,m10
/-MA	delete all markers
/SQ	square vectors (also /SV)
/ST	list indirect gates or boxes
/ST:CU:n	set up indirect gate or box n with cursor
/-ST:n1:n2:....:nm	delete indirect gates or boxes
/-ST	delete all indirect gates or boxes
/WA:val	wait val seconds
/AD:iaddx:iaddy	rebin output
/AN:x1:x2:y1:y2	calc areas, moments
/AN:CUrsor	use cursor to define limits
/BP	bar plots
/DI	get histogram from disk file
/-DI	get histogram from core
/ER	erase screen before plot
/LO	logarithmic z scale
/-LO	linear z scale
/NE	show next plot
/OV	overlay plots
/SH	draw plot
/VP	vector plot
/X:low:high	select x data values to plot
/Y:low:high	select y data values to plot
/Z:low:high	set z scale to given values

Table 2.8: Selected portions of E1140.HST file used to define experiment histograms.

```
;[MP10REP.EXP1140]exp1140.hst
;P3-East  -- LAS High energy DCX
;
/VE:NO
/DE:ALL
/BL:1/OV:-1/DF
;
/VE:BR
/DE:ALL
/BL:1/OV:-1/DF
;
XTGT  /XP:233:-1500:1500:5  /TE:46
THTTGT/XP:234:-2000:2000:10 /TE:46
YTGT  /XP:235:-1000:1000:5 /TE:46
PHITGT/XP:236:-1000:1000:10 /TE:46
;
THTCHK/XP:237:-1000:1000:2   /TE:46
PHICHK/XP:238:-200:200:2   /TE:46
THTSCT /XP:247:-2000:2000:10/TE:46
THSC4 /XP:247·-2000:2000:10/TE:94
THSC5 /XP:247:-2000:2000:10/TE:95
;
MMP    /TE:94/XP:246:-5000:10000:10
;
LRX1 /Xp:23:-100:1200:4/TE:44/bl:1
LRX2 /Xp:24:-100:1200:4/TE:44/bl:1
LRy1 /Xp:25:-100:1200:4/TE:44/bl:1
LRy2 /Xp:26:-100:1200:4/TE:44/bl:1
LRX5 /Xp:27:-100:1200:4/TE:45/bl:1
LRX6 /Xp:29:-100:1200:4/TE:45/bl:1
LRy5 /Xp:28:-100:1200:4/TE:45/bl:1
LRy6 /Xp:30:-100:1200:4/TE:45/bl:1
;
CHER/XP:258:-100:1000:10/TE:93
RF    /TE:93/XP:44:600:800:1
;
S2P/XP:17:0:4000:10/TE:0/BL:1
S2N/XP:18:0:4000:10/TE:0/BL:1
S3P/XP:19:0:4000:10/TE:0/BL:1
S3N/XP:20:0:4000:10/TE:0/BL:1
PID/XP:253:0:2000:40/YP:260:-100:2000:20/BL:1/TE:0
TOF/XP:260:-100:2000:5/BL:1/TE:0
```
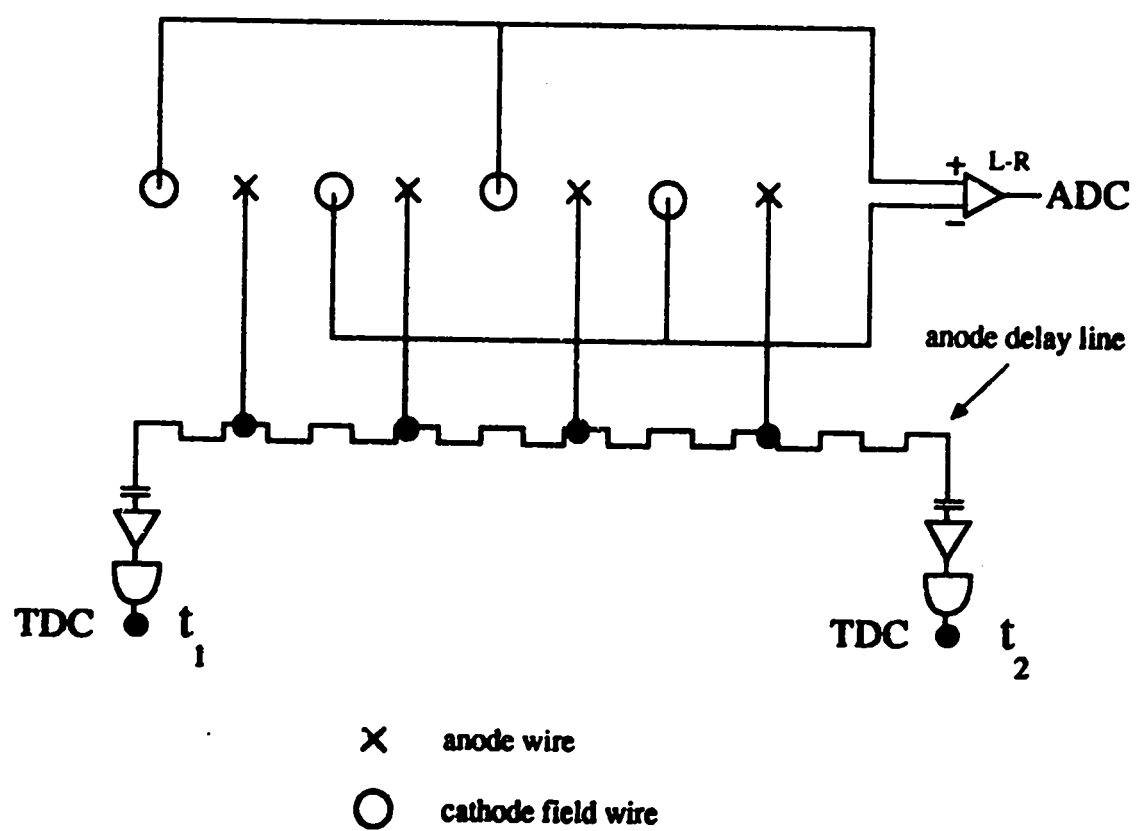
Figure 2.16: A typical MWDC wire chamber.

Chapter 3

Data Analysis

3.1 Replay Procedures

Much of the same methodology used in software calibration before an experiment starts is used during the replay of the data. Off-line replay of data allows the experimenter to fine tune the calibrations run by run. Chamber calibrations can change during an experiment. As the incident pion energy changes, certain timing signals will shift. It is necessary to replay each run carefully and notice when these changes occur. The solution to these problems usually involves re-calibrating drift times or moving an indirect gate or box. In this experiment, it was possible to replay the delta scan to improve the delta polynomial and consequently improve the energy resolution of the spectrometer. The delta polynomial is used for calculating how particles track through the spectrometer when it is set for different δ values.

Another term that is looked at during replay is MMYT, missing mass plotted against YTGT. The MMYT histogram should show a linear, vertical correlation, as shown in Fig. 3.1. The first calibration is made by correcting for the horizontal momentum dispersion across the target. This is done using a heavy target and adjusting the dispersion term, R78, in PRM. Using ^{208}Pb, the horizontal momentum dispersion was found to be,

$$D_y = \frac{\Delta p/p}{\Delta y} = \frac{p_{beam} - p_{channel}}{p_{beam}} = 0.5\%/cm \qquad (3.1)$$

where p_{beam} is the momentum of the beam, measured at a horizontal (y) position on the target. To do this, in software, the trajectory of the scattered particle is projected back to find where it intersects the target, this position is YTGT. The scattered particle momentum is found by measuring the bend angle in the spectrometer. With the beam and scattered particle momentums, along with the scattered particle angle, the kinematics for the two-body interaction in the target can be reconstructed.

There is also an angular dispersion across the target, $dE/d\phi$. By looking at MMYT for a light target, such as ^1H, term 235 (PHIBM) in POL.DAT is varied to remove any further correlations.

The background levels for this experiment are very low. Proton, muon and electron events are easily eliminated with hardware and with software cuts. The ^1H normalization runs have a fairly constant background which can be easily approximated. After these calibrations, all of the events are replayed and the histogram files are summed.

It is important to watch for systematic errors. The digital voltmeter (DVM) that was used to set the LAS dipole shunt voltage was only accurate to two decimal places during some runs. For this reason, only runs where there had been no change in the LAS dipole field were summed together. Normalization runs were taken before and after each series of DCX runs so that the beam conditions would not change appreciably.

3.2 Normalization and Calculations

The DCX differential cross section measured in this experiment is basically a measure of the probability of the reaction $^{18}O(\pi^+,\pi^-)^{18}Ne(DIAS)$ occurring. The number of scattered particles can be written as,

$$N_s = N_b \cdot \Omega \cdot N_t \cdot \frac{d\sigma}{d\Omega}$$ (3.2)

where N_b is the number of incident particles in the beam, N_t is the number of target centers per unit area, Ω is the solid angle seen by the detector, and $d\sigma/d\Omega$ is the differential cross section. The basic geometry used in this description is shown in Fig 3.2. We can solve this equation,

$$\frac{d\sigma}{d\Omega} = \frac{N_s}{N_b \cdot N_t \cdot \Omega}$$ (3.3)

where,

$$N_t = \frac{n \times \rho(g/cm^2)}{M(g/mol)} \times 6.02 \times 10^{23}(mol^{-1}) \times 10^{-27}(cm^2/mb)$$ (3.4)

with ρ being the target density, M, the atomic mass of the target material, and n, the number of target atoms in each molecule of target material. For an $H_2^{18}O$ target, used in the reaction $^{18}O(\pi^+,\pi^-)^{18}Ne(DIAS)$, the total atomic mass is $M = 20$ and since there is one ^{18}O for every $H_2^{18}O$ molecule, $n = 1$.

In this experiment, the DCX runs were normalized to hydrogen, which has well known cross sections. The thin ion chamber was used to normalize the DCX runs. It assured that changes in the beam conditions could be factored out. For each run a NORM was calculated, where

$$NORM = \frac{CF}{IC}$$ (3.5)

and,

$$CF = \frac{|\cos \vartheta_{tgt}|}{LT \cdot CE \cdot LE \cdot SF \cdot d\Omega} \qquad (3.6)$$

and,

θ_{tgt} = Angle of target to beam

CE = Chamber efficiency

LE = Number of loops per event

LT = Computer live time

SF = Survival fraction of pions

$d\Omega$ = Solid angle of spectrometer.

The calculated NORM contains information on solid angle, as well as incident pion flux. It also contains information on the chamber efficiencies, which relate charged particle rates in a chamber with the ability of the chamber to process information. Therefore, by taking the ratio of NORM values in the normalization procedure, it is not necessary to specifically calculate the solid angle of the spectrometer, since they cancel out.

The differential cross section (in the lab frame) is therefore,

$$\frac{d\sigma}{d\Omega_{lab}} \left(\frac{\mu b}{sr}\right) = \frac{Yield_{\nu_0}}{Yield_H} \times \frac{\rho_H/M_H}{\rho_{\nu_0}/M_{\nu_0}} \times \sigma_H \times 10^3 \frac{\mu b}{mb} \qquad (3.7)$$

where,

$$Yield = NORM \times (peak \ counts) \qquad (3.8)$$

$$n_H/M_H = 2/14(g/mol) \tag{3.9}$$

$$n_{18O}/M_{18O} = 1/20(g/mol) \tag{3.10}$$

therefore,

$$\frac{d\sigma}{d\Omega_{lab}}\left(\frac{\mu b}{sr}\right) = \frac{Yield_{18O}}{Yield_H} \times \frac{40\rho_H}{14\rho_{18O}} \times \sigma_H \times 10^3 \frac{\mu b}{mb}. \tag{3.11}$$

The peak counts are taken from the ground state peak in the missing-mass histogram. Missing mass is also called the $-Q$ of the reaction and is determined from the kinematics. Since this experiment could not resolve the ground state (DIAS) peak from other low-lying states, a 7 MeV gate was placed around the prominent DIAS peak for $q = 0$, summing the 0^+ and 2^+ states. The 0^+ and 2^+ states are smoothly varying and it has been assumed that any enhancement of the cross section would be evidenced in the sum of these states. There is also a possible contribution from a $(0^+, 2^+, 4^+)$ triplet near 3.6 MeV, but this contribution should be small and non-varying. As the scattering angle increases, the number of counts in the 0^+ and 2^+ states drops off significantly. Therefore, the number of counts in these states was summed using a 7 MeV gate with the same limits as for the $q = 0$ case. Fig. 3.3 shows how this was done. The hydrogen missing-mass peak was very prominent, as shown in Fig. 3.4. The background level was small and constant, therefore a linear fit to the background was sufficient and the background were subtracted. With the NORM values and the number of counts in the hydrogen and DCX peaks, and using Arndt's values for σ_H from the phase shift analysis program SAID [Ar-83], the last step in extracting the cross sections was to measure the areal densities of the targets. The values of σ_H from SAID are given in Table 3.1, using the SM92 solutions.

The 1991 CH_2 target had an areal density of $\rho_H = 0.294g/cm^2$. The CH_2 target, used in 1992, had an areal density of $\rho_H = 0.288g/cm^2$. The $^1H(\pi^+,\pi^+)^1H$ reaction was measured for both the CH_2 and H_2O targets in 1991. With the yields from these reactions, and knowing the areal density of the CH_2 target was 0.294 g/cm^2, it was possible to cross-normalize and determine the areal density of the H_2O target. Taking into account that there were two windows on the H_2O target, each composed of $\frac{1}{32}$ inch thick CH_2, the yields can be written as,

$$Yield_{H_2O} = \frac{2}{20}\rho_{180} + \frac{2}{14}\left(\frac{2}{32}(in) \times 2.54(\frac{cm}{in})\right) \times \frac{6.02 \times 10^{23}}{10^{27}} \quad (3.12)$$

$$Yield_{CH_2} = \frac{2}{14}\rho_H \times \frac{6.02 \times 10^{23}}{10^{27}}. \quad (3.13)$$

Plugging $Y = 0.294$ g/cm^2 into the ratio of the yields, and setting this equal to the measured ratio,

$$\frac{Yield_{H_2O}}{Yield_{CH_2}} = \frac{\left(\frac{2}{20}\rho_{180} + \frac{2}{14}\left(\frac{2}{32} \times 2.54\right)\right)}{\frac{2}{14}(0.294)} = 4.41 \quad (3.14)$$

we then find,

$$\rho_{180} = 1.62(g/cm^2). \quad (3.15)$$

Dividing through by the isotopic purity of the H_2O, the effective areal density becomes,

$$\rho_{180} = 1.72(g/cm^2). \quad (3.16)$$

To convert the cross sections to the center-of-mass frame, the lab cross section, as given in Eqn. 3.11, is multiplied by the Jacobian. The Jacobian is calculated

from the kinematics, which are listed in Appendix A. The final form used to extract center-of-mass cross sections is,

$$\frac{d\sigma}{d\Omega_{cm}}\left(\frac{\mu b}{sr}\right) = \frac{Yield_{180}}{Yield_H} \times \frac{40\rho_H}{14\rho_{180}} \times \sigma_H \times 10^3 \frac{\mu b}{mb} \times JAC. \qquad (3.17)$$

In order to determine whether the ion chamber was a good method of normalization, comparison was made between the ion chamber and various beamline monitors. The ratio of IC/2ACM02 is shown in Fig. 3.5 for 1991 and in Fig. 3.6 for 1992. Runs with the same MS01 jaw settings are grouped with a solid line in each figure. Only the data taken for $q = 0$ at 350 MeV shows any problem. It was determined that all of the magnet and jaw settings were the same for these runs and that the beam macrostructure had changed. The thin ion chamber was used as the most reliable method of normalizing the beam for these runs.

The statistical uncertainty is calculated using only the number of counts in the DCX and hydrogen peaks. The formula used to find the statistical uncertainty in the cross section is,

$$\varepsilon = \left\{\sqrt{\frac{1}{N_H} + \frac{1}{N_{DCX}}}\right\} \times \frac{d\sigma}{d\Omega}. \qquad (3.18)$$

Further discussion of the propagation of errors in functions is given in Appendix B.
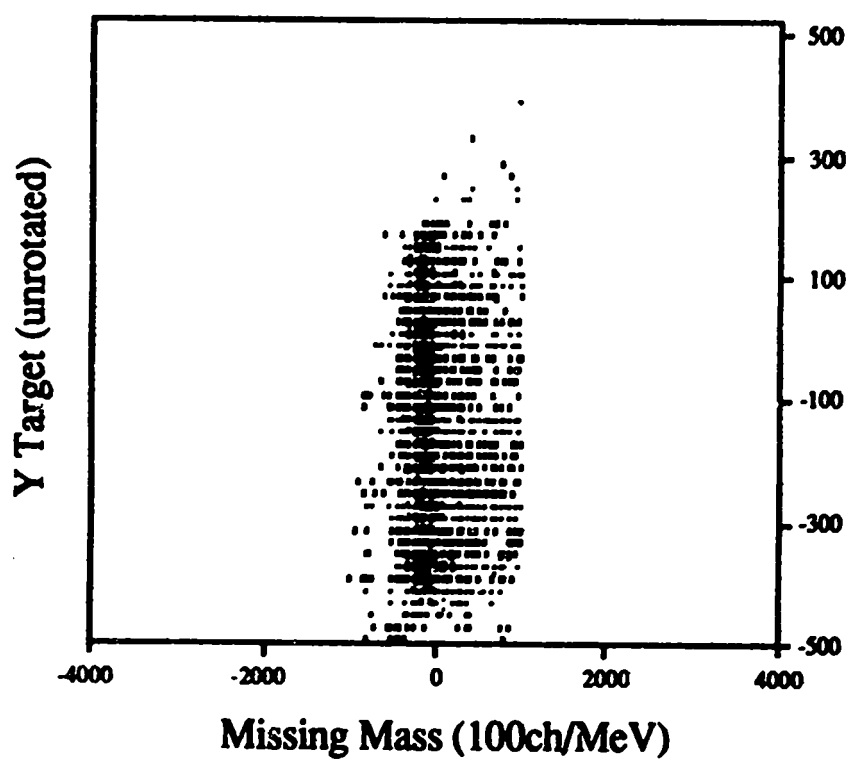
Figure 3.1: A typical MMYT histogram for $^{12}C(\pi^+,\pi^+)^{12}C$ after software calibrations. Missing-mass units are 100 Channels/MeV.

Cross Section

$$\frac{d\sigma}{d\Omega} = \frac{N_s}{N_b N_t \Omega}$$
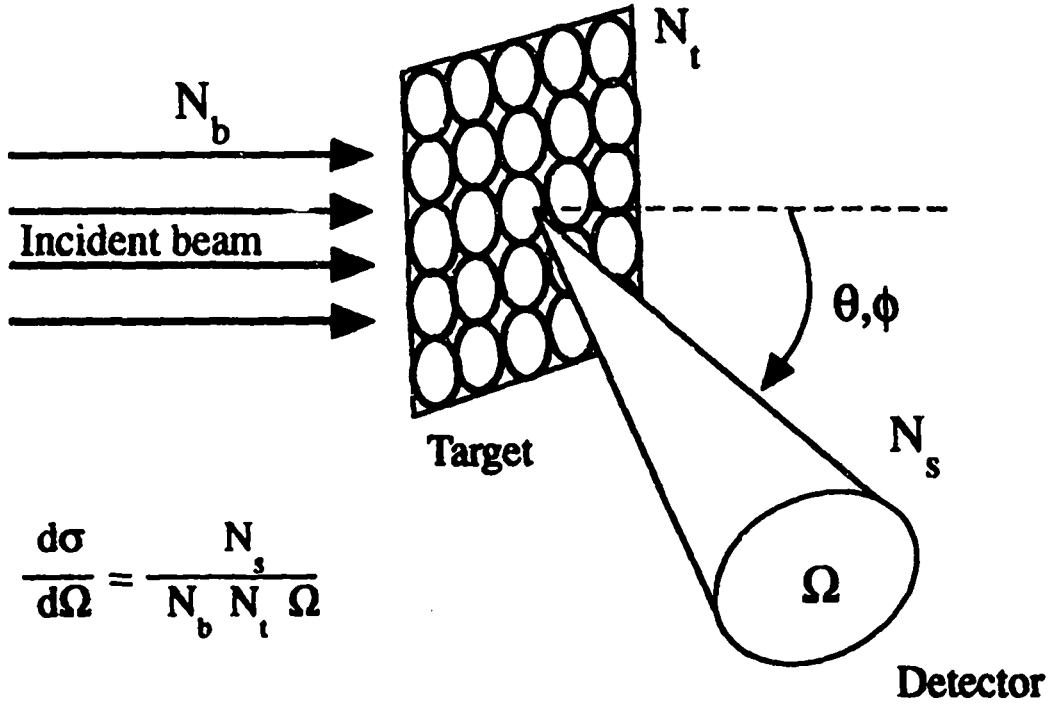
Figure 3.2: Cross section geometry.

Table 3.1: Hydrogen cross sections from Arndt's SAID, using SM92 solutions, for incident π^+.

T_π^{lab}(MeV)	θ_{scat}^{cm}	$\sigma_H^{cm}(\frac{mb}{sr})$	θ_{scat}^{lab}	$\sigma_H^{lab}(\frac{mb}{sr})$
350	55.350	5.683	40.00	9.351
390	56.310	4.498	40.00	7.571
400	56.540	4.258	40.00	7.207
410	56.780	4.034	40.00	6.864
415	56.890	3.930	40.00	6.704
420	57.010	3.827	40.00	6.547
430	57.240	3.634	40.00	6.249
440	57.470	3.453	40.00	5.968
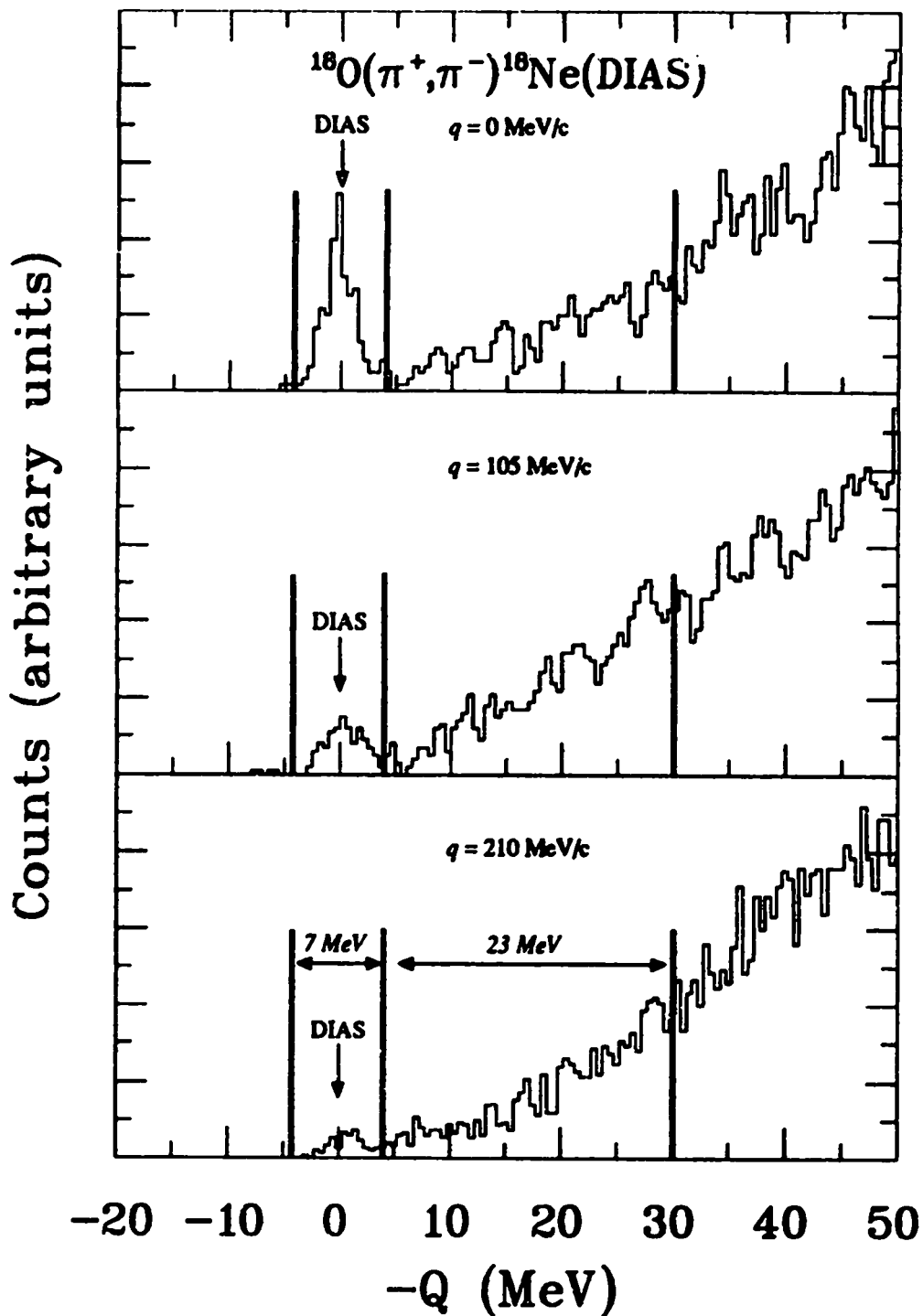
Figure 3.3: $^{18}O(\pi^+,\pi^-)^{18}Ne(DIAS)$ Missing-Mass spectra in arbitrary units at 420 MeV. A 7-MeV gate was set around the centroid of the $q = 0$ MeV/c DIAS peak and the same gate was used for the other momentum transfers.
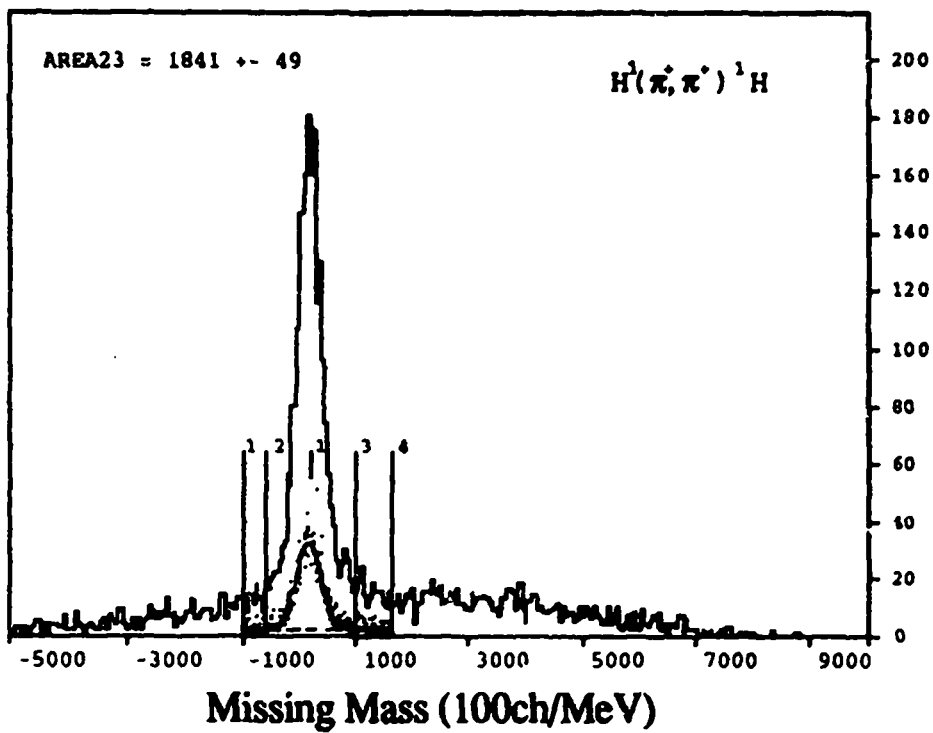
Figure 3.4: Missing-mass histogram for $^1H(\pi^+,\pi^+)^1H$ at 420 MeV. The histogram is shown with an add of 5 bins and the peak fit is shown by a solid line. A linear fit has been made to the background. Missing-mass units are 100 Channels/MeV.
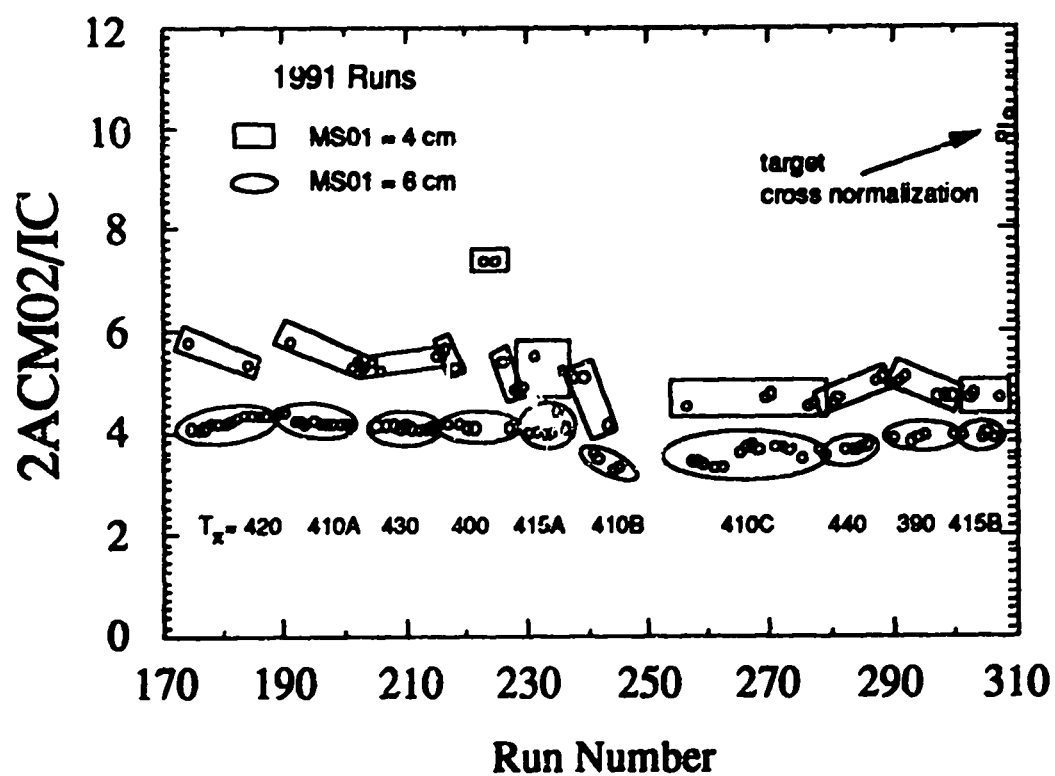
Figure 3.5: Ratio of beamline monitor 2ACM02 to IC for 1991 runs.
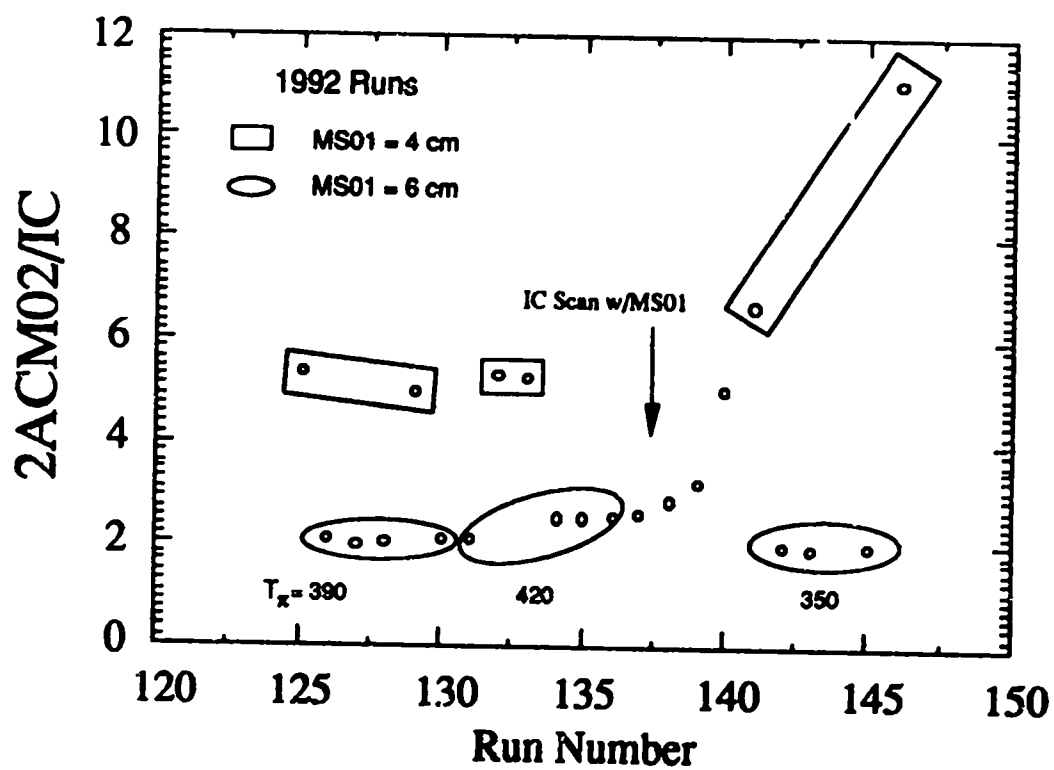
Figure 3.6: Ratio of beamline monitor 2ACM02 to IC for 1992 runs.

Chapter 4

Results

This experiment measured the excitation function for the reaction $^{18}O(\pi^+, \pi^-)^{18}Ne(DIAS)$ over an energy range of $T_\pi = 350 \rightarrow 440$ MeV for fixed momentum transfers of $q=0$, 105, and 210 MeV/c. Table 4.1 lists the center-of-mass differential cross sections and statistical errors, which were extracted using Eqn. 3.17. This data tends to agree with previous cross sections for this energy region within absolute errors of up to 20% [Gr-82, Wi-89].

The $^{18}O(\pi^+, \pi^-)^{18}Ne(DIAS)$ center-of-mass differential cross sections from this experiment are plotted in Fig. 4.1. These results are plotted along with previous data [Gr-82, Wi-89] in Fig. 4.2.

The existence of an η-nucleus bound state should be evidenced by a resonance structure in the excitation function. For this reaction, a peak should be seen for the $q = 210$ MeV/c cross sections at 420 MeV. There is, however, some discussion about the fluctuation ratio and width of such a state. No explicit calculations have been performed for the $^{18}O(\pi^+, \pi^-)^{18}Ne(DIAS)$ reaction. Calculations have been made for the $^{14}C(\pi^+, \pi^-)^{14}O(DIAS)$ reaction, and predict a width of ~10 MeV and a fluctuation ratio of ~79 %. No effect of this order is seen in the cross sections measured by this experiment. Because of the higher density of states for ^{18}O than for ^{14}C, a width greater than 10 MeV is expected. Chiang et al., predict that the width of the ηN bound state for

60
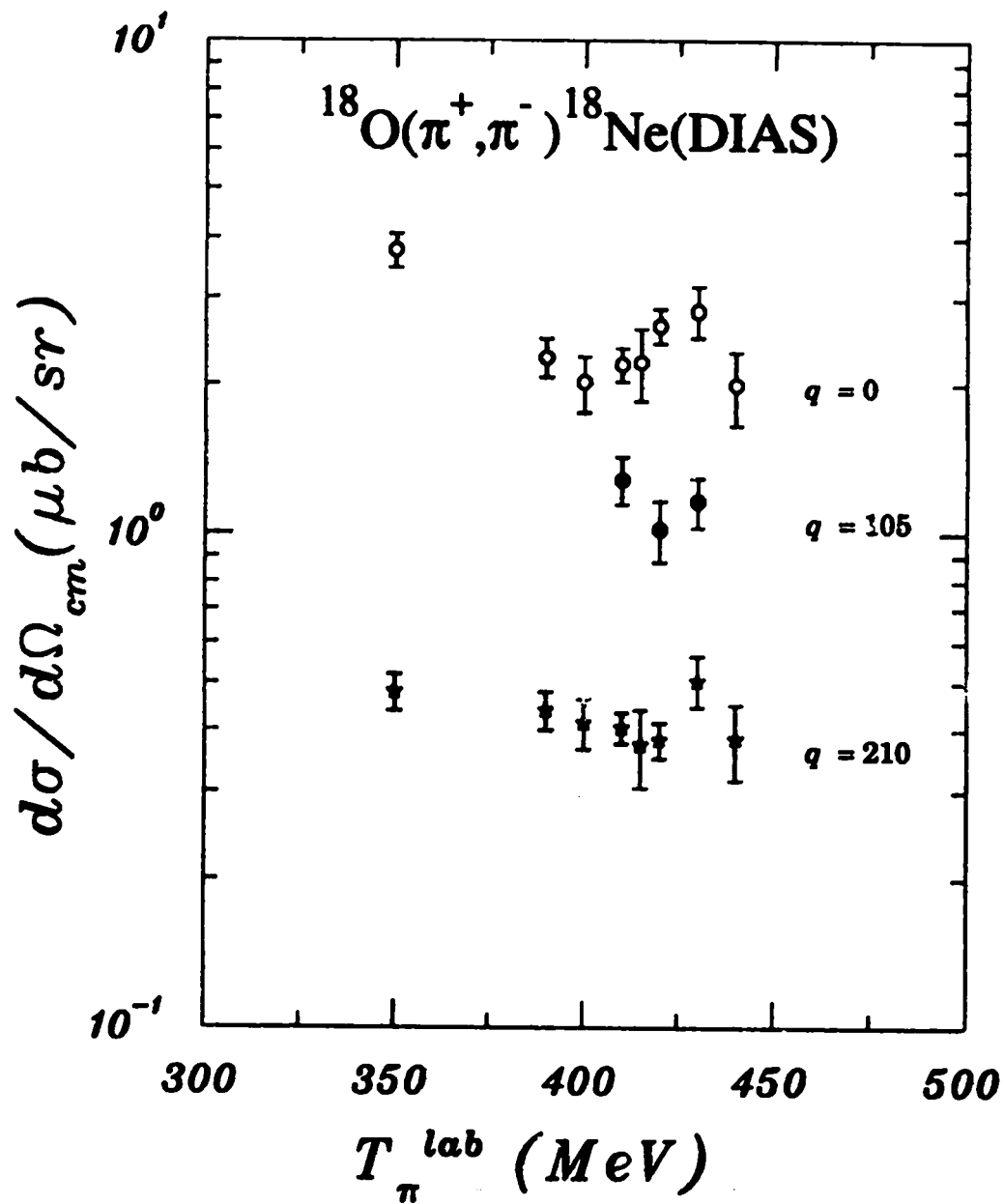
Figure 4.1: Differential cross sections from this experiment for the reaction $^{18}O(\pi^+,\pi^-)^{18}Ne(DIAS)$.
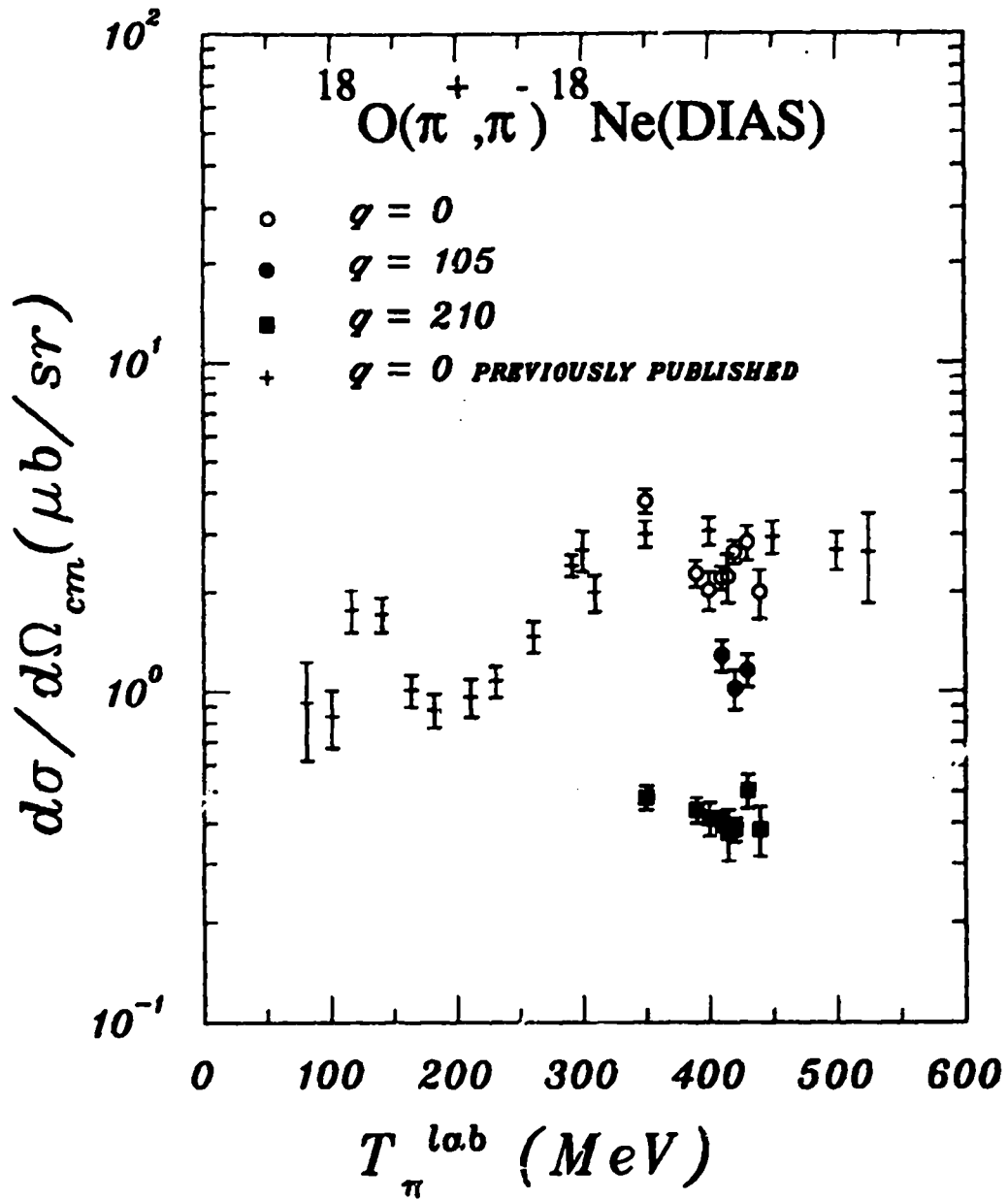
Figure 4.2: Differential cross sections from this experiment and previously published data for the reaction $^{18}O(\pi^+,\pi^-)^{18}Ne(DIAS)$ [Gr-82][Wi-89].

Table 4.1: $^{18}O(\pi^+,\pi^-)^{18}Ne$(DIAS) center-of-mass differential cross sections (μb/sr) using a 7 MeV gate.[a]

T_π	$d\sigma/d\Omega$		
(MeV)	q=0	q=105	q=210 MeV/c
350	3.76 ± 0.30		0.47 ± 0.04
390	2.27 ± 0.20		0.44 ± 0.04
400	2.32 ± 0.16		0.41 ± 0.05
410	2.19 ± 0.17	1.28 ± 0.13	0.40 ± 0.03
415	2.21 ± 0.36		0.37 ± 0.06
420	2.63 ± 0.20	1.01 ± 0.14	0.38 ± 0.03
430	2.81 ± 0.31	1.15 ± 0.13	0.50 ± 0.06
440	1.97 ± 0.32		0.38 ± 0.06

[a] For absolute error add 10% in quadrature

a nucleus like oxygen will be around 30 MeV or larger [Ch-91]. It is expected that the inability to resolve the 0^+, 2^+ and possibly 4^+ states could lead to further widening of a possible ηN bound state [Li-92].

A smoothly varying function is expected for the $q = 0$ MeV/c excitation function, and there seems to be nearly as much structure observed in the $q = 0$ MeV/c cross sections as there is in the $q = 210$ MeV/c data. Previously measured cross sections in this energy region showed no such structure [Gr-82, Wi-89]. The previous data for this region, however, was taken in 50 MeV steps, and may have missed some structure. Most of the experimental errors have been discussed to this point. Although the chamber efficiencies for the wire chambers have been taken into account, the chamber efficiency of the ...... ion chamber, from run to run, has not been included. Fig. 4.3 shows the ratio of the calculated yields from hydrogen normalization runs for jaw settings of MS01 = 4 and 6 cm (1991 data). Several of these points vary from the

expected value of 1 by more than the statistical error. The systematic beam normalization errors can be eliminated by taking the ratio of the $q = 0$ and $q = 210$ MeV/c cross sections. This ratio is shown in Fig. 4.4.

Fig. 4.4 seems to show some structure at the η production threshold of 420 MeV as well as at 350 MeV. The data has been fit with a straight line with $\chi^2/d.f. = 3.44$, indicating the possibility of structure in the region. A check on this method is to look at the ratios of the higher excitation, continuum states. This is done by taking a missing energy bite of 23 MeV above the 7 MeV ground state. A line fit to this coninuum data gives $\chi^2/d.f. = 1.45$. This close agreement with a straight line tends to confirm that we are seeing continuum events from a two-step process as expected. This flat energy dependence also tends to validate the structure seen for the ground state ratios.

There has been some discussion as to why the 350 MeV ground state data is higher than the other points. One suggestion is that as you go down in energy to 350 MeV, you are getting closer to the (3,3) resonance energy, and the pion-nucleus potential grows stronger as the pion absorption radius increases. Such an energy dependence should, however, show up in the ratio of the continuum states. Because there is no such dependence in the continuum states, there is no evidence to support this assumption.

There seems to be no reason for rejecting the 350 MeV data. Careful comparison between beamline monitors and scalers tends to support including this data as long as it is normalized to the thin ion chamber.

One other suggestion, as to the nature of the structure in the ground state data, was that we were observing a cusp effect. A cusp effect is an
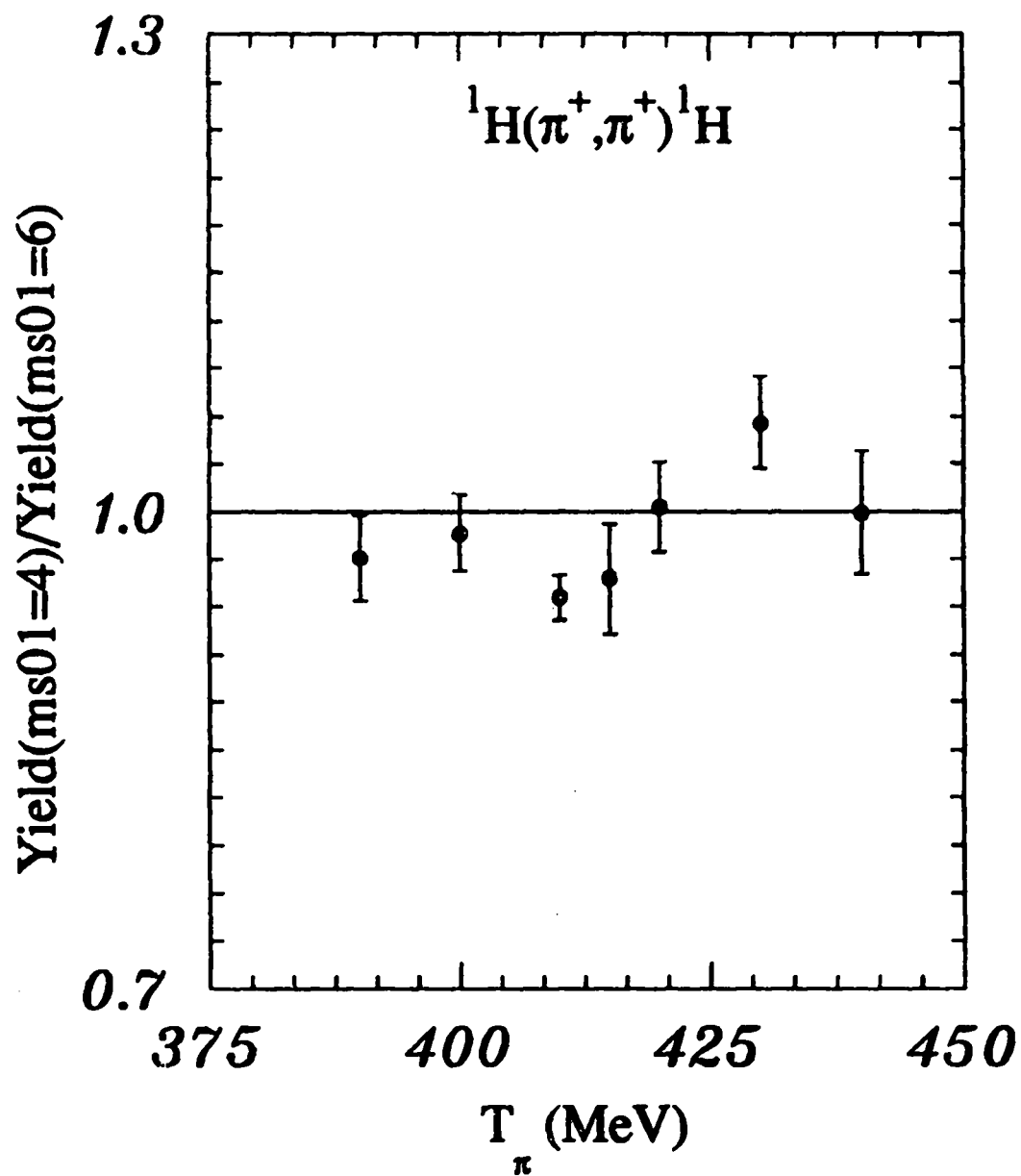
Figure 4.3: Ratios of calculated yields for jaw settings of MS01 = 4 and 6 cm (1991 runs).
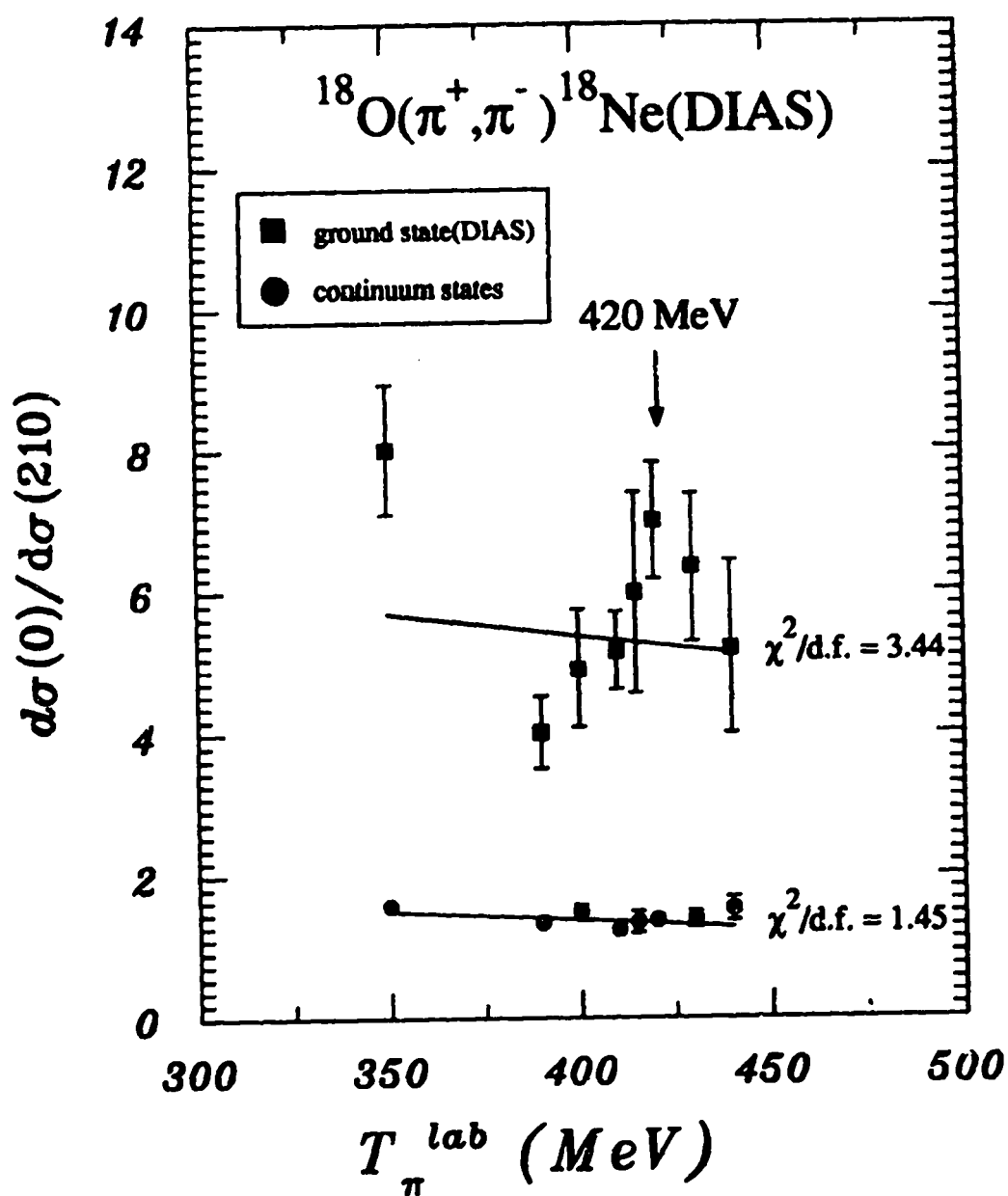
Figure 4.4: Ratios of the $q = 0$ and $q = 210$ MeV/c cross sections plotted with best straight line fits for DIAS and continuum states.

enhancement in the cross section due to the opening of a new reaction channel, in this case the η channel. This effect may possibly contribute to the observed structure, however there is no way to determine the extent of its contribution from this data set. It is doubtful that a cusp effect can explain the enhanced $q = 0$ cross section at 350 MeV.

There is evidence of some structure in the ratio of the $q = 0$ and $q = 210$ MeV/c cross sections near the η production threshold. There is insufficient evidence to attribute this structure to an ηN bound state for this reaction. Because of the statistical precision of this measurement, only a qualitative characterization of this structure is possible. The structure centered at 420 MeV has a maximum fluctuation ratio of $\sim 60\%$ and a width on the order of 25 MeV.

Chapter 5

Theoretical Considerations

5.1   Eta-Nucleus Bound State The r

The ηN interaction has been shown to be attractive for masses $A > 10$.
It is predicted that this interaction could have an important effect on DCX
reactions for energies above 350 MeV. There are two primary channels for pion
DCX reactions in this energy range, $\pi^+ \to \pi^0 \to \pi^-$ and $\pi^+ \to \eta \to \pi^-$.
The π^0 is in the continuum for this process, and the η can exist either in the
continuum or in a strongly bound nuclear state. The continuum states have
a smoothly varying energy dependence, whereas the bound state is predicted
to have a narrow width approximately an order of magnitude smaller than an
unbound πN resonance like the Δ resonance.

An ηN bound state is a doorway state which gives an energy depen-
dence to the cross section. An enhancement to the cross sections should be
evidenced in the excitation function near the η production threshold, which is
$T_\pi \simeq 420\text{MeV}$ for the $^{18}O(\pi^+, \pi^-)^{18}Ne$ reaction.

We can consider this reaction to have initial and final channels repre-
sented by the subspaces a and c. The intermediate channels for the and the
η-nuclear states are represented by the subspaces b_1 and b_2 respectively. The
states representing quasifree one-nucleon processes and true meson absorption
are represented by the subspace Q. With this formalism in mind, the cross

68

section for DCX reactions can be written as [Ha-87],

$$\frac{d\sigma}{d\Omega} = (2\pi)^4 \mu(k)\mu(k')\frac{k'}{k} \left|\left\langle \xi_{c,k'}^{(-)} |U_{ca}(W)| \xi_{a,k}^{(+)}\right\rangle\right|^2 \tag{5.1}$$

where,

$$k = \text{initial pion momentum (c.m.)}$$

$$k' = \text{final pion momentum (c.m.)}$$

$$\mu(k) = \left(\frac{E_\pi(k)E_A(k')}{E_\pi(k) + E_A(k')}\right)$$

$$\xi = \text{distorted wave operators in channels a and c.}$$

Because the η has zero isospin and because there are an equal number of protons and neutrons in the intermediate state, ^{18}F, we can take, $\tilde{V}_{b_1 b_2} = \tilde{V}_{b_2 b_1} = 0$. The DCX transition operator becomes,

$$U_{ca} = \tilde{V}_{ca} + \tilde{V}_{cb_1} G_{b_1}^{(+)} \tilde{V}_{b_1 a} + \tilde{V}_{cb_2} G_{b_2}^{(+)} \tilde{V}_{b_2 a}. \tag{5.2}$$

Here $G_j^{(+)} = (W - K_j - \tilde{V}_{jj} + i\epsilon)^{-1}$ is the Green's function in some channel j, where $W = E_\pi(k) + E_A(k')$ is the total energy and K_j is the channel kinetic energy operator for the channel. The only Q space contribution in our energy range is due to true meson absorption, which is small. Also, the a and c channels differ by two units of charge, so $V_{ca} \equiv 0$ and the many-body operator,

$$\tilde{V}_{ca} = V_{ca} + V_{cQ}(W - K_Q - V_{QQ} + i\epsilon)^{-1}V_{Qa} \longrightarrow 0. \tag{5.3}$$

Therefore,

$$U_{ca} \simeq \tilde{V}_{cb_1} G_{b_1}^{(+)} \tilde{V}_{b_1 a} + \tilde{V}_{cb_2} G_{b_2}^{(+)} \tilde{V}_{b_2 a} \qquad (5.4)$$

where $\tilde{V}_{ij}$ are the meson-nucleon t-matrices. The Green's functions can be decomposed,

$$G_{b_1}^{(+)}(W) = \sum_\alpha \int d\mathbf{p} \, |\psi_{\pi^\circ,p,\alpha}^{(+)}\rangle [W - E_{\bar{\pi}}(\mathbf{p}) - E_\alpha + i\epsilon]^{-1} \langle \Psi_{\pi^\circ,p,\alpha}^{(+)}| \qquad (5.5)$$

$$G_{b_2}^{(+)}(W) = \sum_\alpha \int d\mathbf{p} \, |\psi_{\eta^\circ,p,\alpha}^{(+)}\rangle [W - E_\eta(\mathbf{p}) - E_\alpha + i\epsilon]^{-1} \langle \Psi_{\eta^\circ,p,\alpha}^{(+)}|$$
$$+ \sum_\beta |\phi_\beta\rangle \left(W - \left[M_\eta + M_A - B_\beta^\eta - (i/2)\Gamma_\beta^\eta\right]\right)^{-1} \langle \Phi_\beta|. \qquad (5.6)$$

In these equations, α represents the extra quantum numbers needed to for the intermediate states with energies E_α, and β represents the ηN bound states with energies E_β, and widths Γ_β^η. The second term in $G_{b_2}^{(+)}$ is used describe the formation of the ηN state. And, $|\psi\rangle \langle\Psi|$ and $|\phi\rangle \langle\Phi|$ are projectors constructed from the scattering and bound state wave functions.

In order to estimate the width of an ηN state it is necessary to evaluate the η-nucleus optical potential. The lowest-order ηN optical potential results from interactions with a single nucleon [Gi-85a]. This potential is proportional to the density, ρ. Higher-order effects are caused by two-nucleon interactions and proportional to ρ^2. Unlike the low-energy πN optical potential, the ρ^2 interaction is not important for the ηN optical potential [Ha-86]. This is true since $M_\eta \simeq 4M_\pi$, making η absorption less kinematically likely.

The ηN optical potential been calculated for the $^{14}C(\pi^+,\pi^-)^{14}O$(DIAS) reaction. The predicted resonance effect has a width of $\sim$ 11 MeV centered

at $T_\pi = 419$ MeV with a fluctuation ratio of $\sim 79\%$ for a momentum transfer of $q = 210\text{MeV/c}$. The solution of the ηN optical potential becomes much more complicated for the $^{18}\text{O}(\pi^+, \pi^-)^{18}\text{Ne}$(DIAS) reaction. Measurements of the width and fluctuation ratio of the ηN resonance for this reaction should yield information on the ηN interaction and lead to a better understanding of the ηN potential. The results of this experiment estimate the width of this resonance as ~ 25 MeV and the fluctuation ratio as $\sim 60\%$.

This section is only inter ded as a brief introduction to the formulation of the DCX cross section and the ηN interaction. Much of this work comes from the reference [Ha-87]. Additional sources of information can be found in the references [Ha-86, Ch-91].

5.2 The Compound Nucleus and Resonance Effects

Early neutron scattering experiments showed empirically that the density of states for the slow neutron capture reaction on targets with $A \sim 100$, was six orders of magnitude greater than predicted for single-particle motion [Bo-69]. The observed level densities were attributed to a complex nuclear state where the neutron shares its energy with the many possible configurations inside the nucleus. The mixing of stationary and resonance states leads to a complex state called the compound nucleus. In a similar manner to the low-energy neutron-induced resonance, interference between channels in the DCX reaction can lead to the formation of a mesic compound nucleus for incident pion energies of $T_\pi > 400$ MeV [Ha-87]. These resonances are due to the decay of metastable states, formed in the initial stage of the reaction. They can be

referred to as *doorway states*, which decay partly into open channels and partly through coupling to the internal degrees of freedom in the compound nucleus [Bo-69].

Resonance effects have been studies in nuclear physics for many years. Resonances provide a way of studying intermediate nuclear states and interactions that cannot be studied directly. The well known ρ resonance, for example, has been studied by making measurements on the reaction $\pi + N \to 2\pi + N$ [Ta-72]. The $\Delta_{3/2,3/2}(1236)$ is another well studied resonance. A prominent peak is seen in the total cross section for $\pi + p$ at an incident pion energy of $T_\pi \sim 190$ MeV. This resonance is shown in Fig. 5.1 for incident π^+ and π^- [Pr-90].

The measurement of a sharp variation in the cross section at a resonance energy, E_R, is evidence of a *nearly bound* metastable state. For a simple scattering reaction the scattering matrix is written,

$$ \mathcal{S} = \langle \mathbf{p}' | \mathbf{S} | \mathbf{p} \rangle \tag{5.7} $$

where

$$ \mathbf{S} | \Psi_{in} \rangle = | \Psi_{out} \rangle \tag{5.8} $$

In general, if the pole of the S-matrix exists in the upper half plane, $\{Im(p) > 0\}$, it corresponds to a bound state with angular momentum l. A pole in the lower half plane, $\{Im(p) < 0\}$, corresponds to a resonance with angular momentum l. As the entrance channel energy increases, a pole, on the threshold between planes, goes from being a virtual state, or resonance, to a bound state. If we make the assumption that the S-matrix has a simple isolated pole in the lower
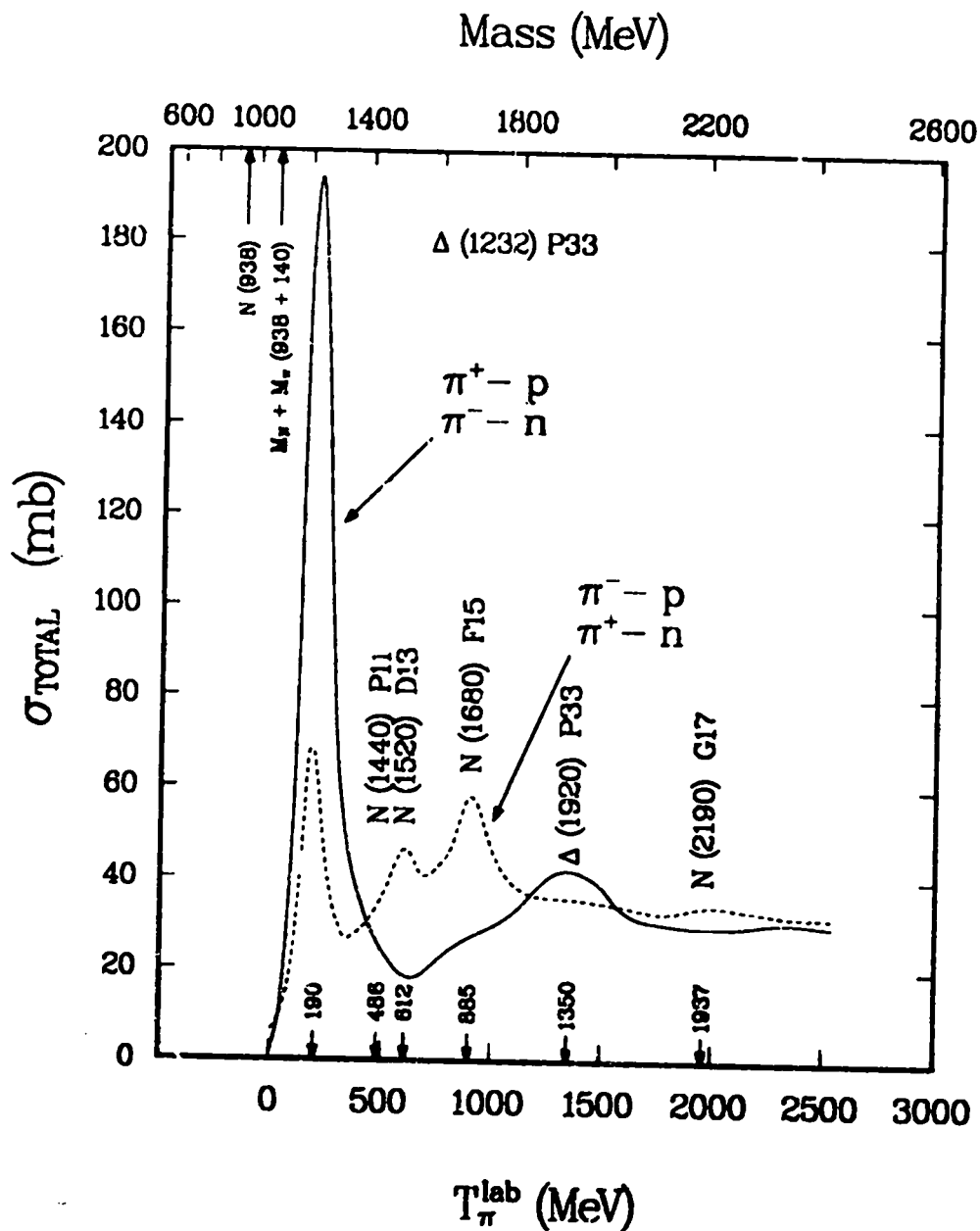
Figure 5.1: Total cross sections for πN scattering as a function of energy. Taken from [PR-90]. The $\Delta_{3/2,3/2}$ resonance is shown at 190 MeV.

half plane, we can write it as [Ta-72],

$$S = 1 - \frac{iA}{E - E_R + i\Gamma/2} \qquad (5.9)$$

the $n \times n$ open-channel S-matrix, where E_R is the resonance energy, Γ is the width of the resonance, and A is the residue matrix for this pole. This form of the S-matrix is also based on the assumption that the behavior of the interaction amplitude is similar to the *Breit-Wigner* form,

$$f_{\alpha'\alpha} = \frac{-1}{2(p_{\alpha'}p_\alpha)^{1/2}} \frac{a_{\alpha'\alpha}}{E - E_R + i\Gamma/2} \qquad (5.10)$$

for E near E_R. Here α represents the entrance channel, α' represents the exit channel, and the residue, $a_{\alpha'\alpha}$, is constrained by the requirement that S be unitary. The possible resonance shapes for this simple formulation are shown in Fig. 5.2 for an isolated pole at $E_R - i\Gamma/2$ for the entrance channel. The solid lines represent total cross sections, σ_{tot}^l, and the dashed lines represent the elastic cross sections, σ_{el}^l for angular momentum l.

At the threshold energy for the opening of a new reaction channel, it is also possible to see an enhancement to the partial cross sections in the shape of a cusp or rounded step, as shown in Fig. 5.3. This occurs when the partial cross sections are coupled to the nuclear s-wave state by angular momentum and parity conservation.

This section has been a brief introduction to the terminology used to describe the compound nucleus and resonance effects. A more formal and in-depth discussion of scattering theory and resonances can be found in the references [Ne-82, Ro-67, Ta-72].
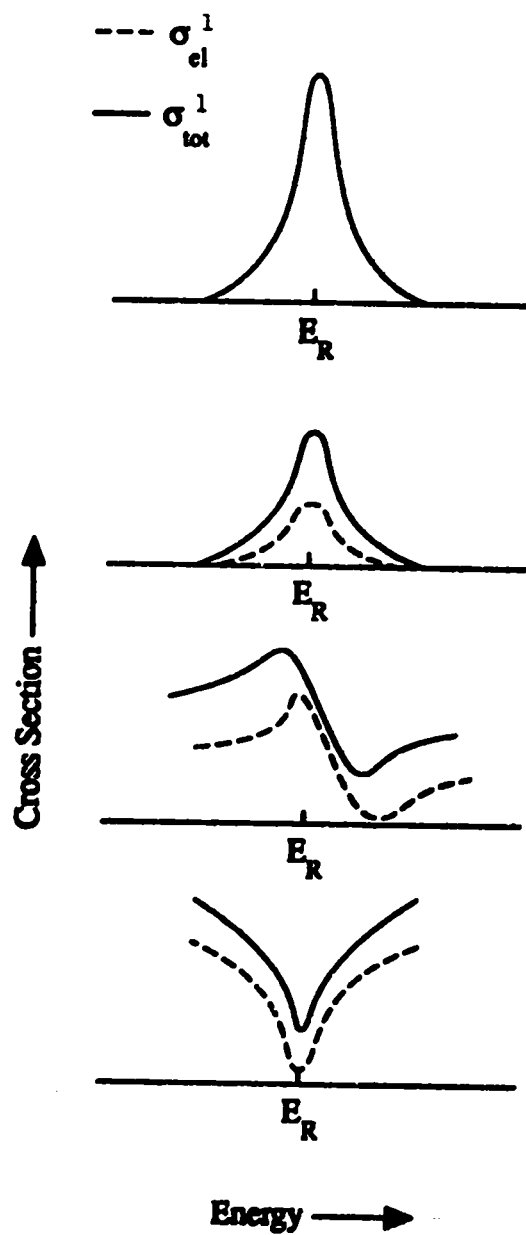
Figure 5.2: Possible resonance shapes for an isolated pole at $E_R - i\Gamma/2$ for the entrance channel [Ta-72].

Threshold Effects
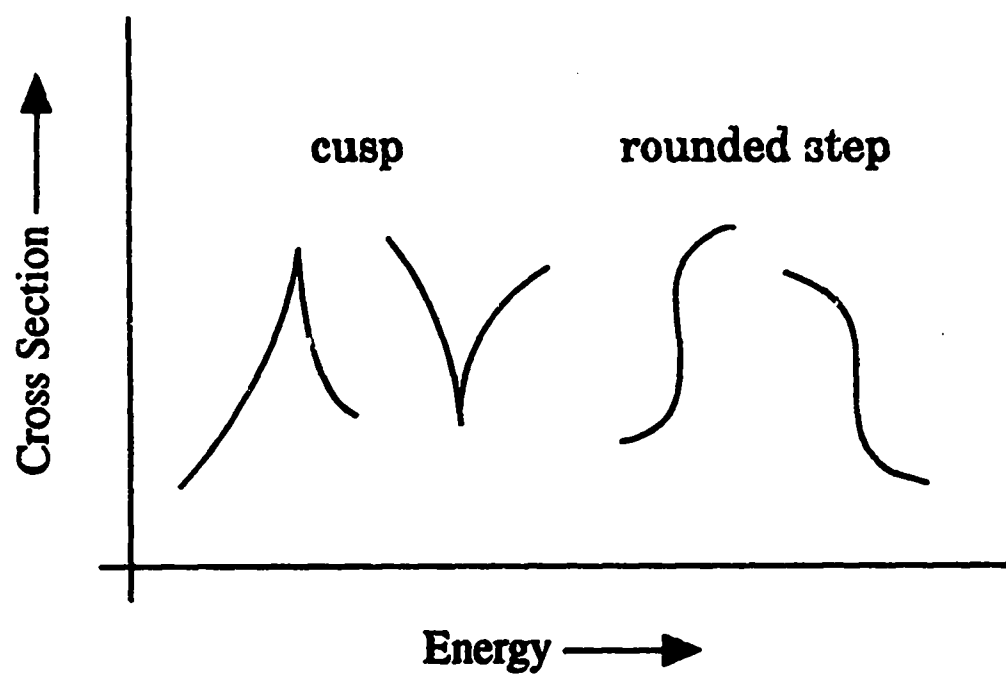

Figure 5.3: Cusp and rounded step shapes due tc the opening of a new reaction channel [Ne-82].

Appendix A

Kinematics Tables

Table A.1: ^{18}O DCX kinematics used in E1140.

T_π(MeV)	Θ_c^{lab}	Θ_c^{cm}	T_c^{lab}(MeV)	p_c^{lab}	β_c	$1/vc$(ns/m)	JAC
350.000	25.86	26.58	343.62	462.60	0.957	3.484	0.950
389.853	23.73	24.45	383.47	504.08	0.964	3.461	0.946
399.853	23.25	23.97	393.47	514.45	0.965	3.456	0.944
409.853	22.79	23.52	403.47	524.80	0.966	3.452	0.943
414.853	22.57	23.29	408.47	529.97	0.967	3.449	0.943
419.853	22.35	23.07	413.47	535.14	0.968	3.447	0.942
429.853	21.93	22.65	423.47	545.47	0.969	3.443	0.941
439.853	21.52	22.23	433.47	555.79	0.970	3.439	0.940

Table A.2: Hydrogen kinematics used in E1140.

T_π(MeV)	Θ_c^{lab}	Θ_c^{cm}	T_c^{lab}(MeV)	p_c^{lab}	β_c	$1/vc$(ns/m)	JAC
350.000	40.00	55.35	300.98	417.86	0.948	3.517	0.608
389.853	40.00	56.31	332.30	450.76	0.955	3.492	0.594
399.853	40.00	56.54	340.08	458.89	0.957	3.487	0.591
409.853	40.00	56.78	347.82	466.97	0.958	3.481	0.588
414.853	40.00	56.89	351.67	471.00	0.959	3.479	0.586
419.853	40.00	57.01	355.52	475.01	0.959	3.477	0.585
429.853	40.00	57.24	363.19	483.00	0.961	3.472	0.582
439.853	40.00	57.47	370.83	490.95	0.962	3.468	0.579

Appendix B

Error Propagation

This section is intended as a brief summary on how errors were propagated for this experiment and on how to propagate errors in a general function. The only errors quoted for this experiment are statistical. For absolute errors, it is necessary to add 10% in quadrature. More information on error analysis can be found in the reference [Be-69].

In general, when you want to propagate errors in a function (assuming that there is no covariance between variables) the variance is given by:

$$\sigma_x^2 \simeq \sigma_u^2 \left(\frac{\partial x}{\partial u}\right)^2 + \sigma_v^2 \left(\frac{\partial x}{\partial v}\right)^2 + \cdots$$

The following are specific examples.

Addition or Subtraction

$$x = u \pm v \qquad\qquad\qquad\text{(B.1)}$$

$$\sigma_x^2 = \sigma_u^2 + \sigma_v^2 \qquad\qquad\qquad\text{(B.2)}$$

Multiplication

$$x = uv \qquad\qquad\qquad\text{(B.3)}$$

$$\sigma_x^2 = \left(v^2\sigma_u^2 + u^2\sigma_v^2\right)x^2 \qquad\qquad\qquad\text{(B.4)}$$

Division

$$x = u/v \qquad \text{(B.5)}$$

$$\sigma_x^2 = \left(\sigma_u^2/u^2 + \sigma_v^2/v^2\right) x^2 \qquad \text{(B.6)}$$

Powers

$$x = u^{\pm b} \qquad \text{(B.7)}$$

$$\sigma_x = xb\frac{\sigma_u}{u} \qquad \text{(B.8)}$$

Exponentials

$$x = e^{\pm bu} \qquad \text{(B.9)}$$

$$\sigma_x = xb\sigma_u \qquad \text{(B.10)}$$

$$\text{(B.11)}$$

$$x = a^{\pm bu} \qquad \text{(B.12)}$$

$$\sigma_x = x(b\ln a)\sigma_u \qquad \text{(B.13)}$$

Logarithms

$$x = a\ln(\pm bu) \qquad \text{(B.14)}$$

$$\sigma_x = a\frac{\sigma_u}{u} \qquad \text{(B.15)}$$

Appendix C

Dissertation Publications

Publications resulting from this work are:

Search for an η bound state in pion DCX on ^{18}O

(This paper was submitted to Phys. Rev. C on November 5, 1992.)

Search for an η bound state in pion DCX on ^{18}O

J. D. Johnson[1], G. R. Burleson[4], C. Edwards[5], M. El-Ghossain[4],

M. A. Espy[5], R. Garnett[3], A. Hussein[2], K. Johnson[1], C. F. Moore[1],

C. L. Morris[3], J. M. O'Donnell[3], M. Palarczyk[5], M. Rawool-Sullivan[3,4],

H. Ward[1], D. Watson[7], C. Whitley[1], and A. L. Williams[6]

[1] The University of Texas at Austin, Austin, Texas 78712

[2] King Fahd University of Petroleum and Minerals, Dhahran 31261 Saudi Arabia

[3] Los Alamos National Laboratory, Los Alamos, New Mexico 87545

[4] New Mexico State University, Las Cruces, New Mexico 88003

[5] University of Minnesota, Minneapolis, Minnesota 55455

[6] University of Pennsylvania, Philadelphia, Pennsylvania 19104

[7] University of York, York Y01-5DD, United Kingdom

The search for an eta bound state in the DCX reaction $\pi^+ \quad)^{18}$Ne(DIAS) has been carried out at LAMPF using the P^3 channel and the LAS spectrometer. An excitation function for this reaction was measured for energies ranging from 350 MeV to 440 MeV and for momentum transfers of 0, 105 and 210 MeV/c. The measured cross sections tend to agree with previous results for DCX on ^{18}O. The measured excitation function shows some evidence for structure near the eta production threshold.

PACS numbers: 25.80.Gn, 27.20+n

Coupled-channel calculations by Bhalerao and Liu have shown that the η-N interaction is attractive for nuclei with $A \geq 12$[1]. Recent calculations by Haider and Liu[2] have predicted that a bound state between an eta and a nucleus may occur as an intermediate state in pion double charge exchange (DCX). Such an effect would compete with π^0 and η channels in the continuum. The existence of such a mesic nucleus would lead to a resonance-like structure in the DCX excitation function at fixed momentum transfer, due to the interference between these channels. Calculations made for the reaction $^{14}C(\pi^+, \pi^-)^{14}O(DIAS)$ predict that this structure should occur with a fluctuation ratio of $(\sigma_{max} - \sigma_{min})/\sigma_{average} \sim 79\%$ for DCX reactions at a momentum transfer of $q = 210$ MeV/c[2]. It should occur at the eta production threshold with a width on the order of 10 MeV and add to the smoothly varying continuum amplitude. It should be noted that because of the greater level density compared to ^{14}C, the fluctuation ratio for ^{18}O may be smaller. Chiang et al., predict that the width of the eta bound state for a nucleus like oxygen will be around 30 MeV or larger[3]. If the width is larger than the 10 MeV predicted for ^{14}C then the fluctuation ratio will also be smaller. Haider and Liu[2] note that if the width is a factor of four greater than the factor of 10 MeV expected, the fluctuation ratio should still be $\sim 20\%$ at $q = 210$ MeV/c. For the reaction $^{18}O(\pi^+, \pi^-)^{18}Ne$ the eta threshold occurs when the eta is bound in the first nuclear orbital of ^{18}F[2]. Taking into account the excitation energy to the IAS (T=1) state in ^{18}F, the resonance effect should be seen at 420 MeV.

Lieb et al.[4], have seen possible evidence of an eta bound state from studies of the reaction $A(\pi^+, p)\eta A - 1$. However, Chrien et al.[5], found no evidence of the creation of an eta bound state with width ~ 9 MeV, but their upper limit, for a fluctuation ratio $\frac{f}{}$ of the predicted size, is larger than that estimated by Liu. This paper reports an attempt to

confirm this new type of nuclear matter with an experiment at LAMPF devised to search for an η-nucleus bound state in the DCX reaction $^{18}O(\pi^+,\pi^-)^{18}Ne$. The excitation function for this reaction was measured for momentum transfers of $q = 0$, 105, and 210 MeV/c for energies ranging from $T_\pi = 350$ to 440 MeV.

This experiment was carried out using the Large Acceptance Spectrometer (LAS) in the P^3 East channel at LAMPF, as configured for DCX measurements[6,8]. The P^3 channel was tuned for a dispersed beam with a beam spot of about 2.5 cm (horizontal) $\times$ 3.5 cm (vertical) and an energy resolution of 0.15%, delivering approximately $1 - 2 \times 10^7$ pions/s to the LAS spectrometer.

The LAS spectrometer consists of a C-magnet, a quadrupole doublet, a dipole magnet, two pairs of drift chambers, a Cherenkov detector, and two scintillators. To minimize multiple scattering, helium bags were installed after the target chamber and through to the rear chamber. The C-magnet was used to sweep away protons and positive pions and gave a 10° horizontal bend to particles with momentum matched to the spectrometer. The LAS dipole has a 45° bend, an acceptance of $\pm$ 10%, a dispersion of $\delta p/p = 2$ cm/%, and it subtends a maximum solid angle of ~ 10 msr. There was one pair of delay-line readout drift chambers located before and one pair after the dipole, which were used for particle tracking. The gas threshold Cherenkov detector contained isobutane and was used to eliminate electron events. Two scintillators were used to determine time of flight for particle identification. The hardware trigger required that both scintillators fire in coincidence with either of the front chambers. The incident pion flux was monitored by a thin ion chamber immediately upstream of the target chamber. Measurements were carried out both in 1991 and 1992.

The target was liquid H_2O with an isotopic purity for ^{18}O of 94%. The active area of

4

the target measured 6.66 cm (horizontal) × 7.56 cm (vertical), and the target windows were made of 0.1588-cm CH_2. By using both CH_2 and ^{18}O targets with hydrogen kinematics, it was possible to cross-normalize and experimentally determine the ^{18}O target areal density. After taking into account the isotopic purity, the ^{18}O areal density was 1.72 g/cm^2. The CH_2 areal density was measured to be 0.294 and 0.288 g/cm^2 for the 1991 and 1992 runs respectively.

DCX runs for the reaction $^{18}O(\pi^+,\pi^-)^{18}Ne$ were taken at $5°$ ($q \approx 0$) and for fixed momentum transfers of $q = 105$ and 210 MeV/c. Normalization measurements were made for DCX runs at each energy using the CH_2 target with hydrogen kinematics at $40°$. Normalization runs at a particular energy were taken before or after the DCX runs at that energy. The only difference between DCX runs at a particular energy was the spectrometer and target angles and beamline jaw settings. This should be a consistent and robust method of determining yields and cross sections.

The cross section for the low-lying 2^+ state in ^{18}O increases significantly with angle relative to the ground state, and there is also a possible contribution from a (0^+, 2^+, 4^+) triplet near 3.6 MeV. With an experimental resolution of 2.3 MeV (FWHM), it is not possible to resolve the ground state (DIAS) from the low-lying states, therefore no attempt to separate these states was made. The results reported here for $q = 0$, were obtained by summing counts inside of 7 MeV placed around the 0^+ and 2^+ states in the r'ising-mass histogram. For higher momentum transfers, the number of counts in the 0^+ and 2^+ states drops off significantly, therefore the number of counts in these states was determined by setting a 7-MeV gate in the same position as for the $q = 0$ case. Fig. 1 shows missing-mass histograms for ^{18}O for $q = 0$, 105, 210 MeV/c, with a 7-MeV gate set as described above. The error in

using this method to determine the number of counts is less than 5%. Elastic scattering of π^+ on ^{1}H was measured at each energy and absolute normalizations were obtained from the phase-shift program of Arndt, SAID[7].

The calculated cross sections were found to agree with previously published data in this energy range[8, 9], which also did not separate the ground state from adjacent states. The cross sections determined in this experiment are listed in Table I and plotted in Fig. 2 along with previously published results for the ^{16}O$(\pi^+,\pi^-)^{16}$Ne(DIAS) reaction.

Systematic normalization errors can be reduced by taking a ratio of the $q = 210$ to $q = 0$ MeV/c cross sections. Beam normalization errors will cancel in this ratio. A check of this assumption is provided by the data in the unbound region of ^{16}Ne. For these states there should be no structure, as the mechanism involved is clearly a two-step process. The solid circles in Fig. 3 show this ratio for a missing energy bite of 23 MeV above the ground state. A fit to the data with a straight line gives $\chi^2/d.f. = 1.45$. Within errors this ratio is a constant function of beam energy. The ratio for the bound-state region is shown by solid squares in Fig. 3. The fit to the data with a straight line gives $\chi^2/d.f. = 3.44$, indicating here may be structure in the eta threshold region. Unfortunately the statistical precision of the data is not sufficient to allow more than a qualitative characterization of this effect. The maximum fluctuation ratio in the data is $\sim 60\%$ for a peak centered near 420 MeV and with a width on the order of 25 MeV.

REFERENCES

[1] Q. Haider and L. C. Liu, Phys. Lett. 172B, 257 (1986).

[2] Q. Haider and L. C. Liu, Phys. Rev. C 36, 1636 (1987).

[3] H. C. Chiang et. al., Phys. Rev. C 44, 738 (1991).

[4] B. J. Lieb et. al. in Progress at LAMPF, 1988 (unpublished).

[5] R. E. Chrien et. al., Phys. Lett. 60B, 2595 (1988).

[6] A. L. Williams, Ph. D. thesis, University of Texas at Austin, Los Alamos report LA-12209-T (1991).

[7] R. Arndt, computer code SAID, Phys. Rev. D 28, 97 (1983), Winter 1992 solutions.

[8] A. L. Williams et. al., Phys. Lett. 216B, 11 (1989).

[9] S. J. Green et. al., Phys. Rev. C 25, 927 (1982) and P. A. Seidl et. al., Phys. Lett. 154B, 255 (1985).

FIGURES

FIG. 1.   Missing-Mass spectra in arbitrary units for the reaction $^{18}O(\pi^+,\pi^-)^{18}Ne$(DIAS) at 420 MeV. A 7-MeV gate was set around the centroid of the $q = 0$ MeV/c DIAS peak and the same gate was used for the other momentum transfers.

FIG. 2.   Differential cross sections from this experiment and previously published data for the reaction $^{18}O(\pi^+,\pi^-)^{18}Ne$(DIAS).

FIG. 3.   Ratios of the $q = 0$ and $q = 210$ MeV/c cross sections plotted with best straight line fits for DIAS and continuum states.

TABLES

TABLE I. The center-of-mass differential cross sections (μb/sr) for $^{18}O(\pi^+,\pi^-)^{18}Ne$(DIAS) using a 7-MeV gate.[a]

T_π	$d\sigma/d\Omega$		
(MeV)	$q=0$	$q=105$	$q=210$ MeV/c
350	3.76 ± 0.30		0.47 ± 0.04
390	2.27 ± 0.20		0.44 ± 0.04
400	2.32 ± 0.16		0.41 ± 0.05
410	2.19 ± 0.17	1.28 ± 0.13	0.40 ± 0.03
415	2.21 ± 0.36		0.37 ± 0.06
420	2.63 ± 0.20	1.01 ± 0.14	0.38 ± 0.03
430	2.81 ± 0.31	1.15 ± 0.13	0.50 ± 0.06
440	1.97 ± 0.32		0.38 ± 0.06

Fig. 1

$^{18}O(\pi^+,\pi^-)^{18}Ne(DIAS)$

DIAS $q = 0$ MeV/c

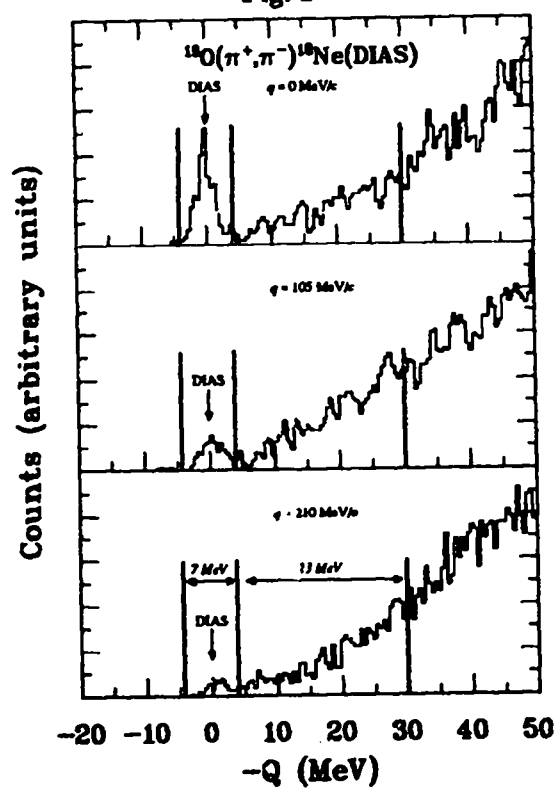$q = 105$ MeV/c
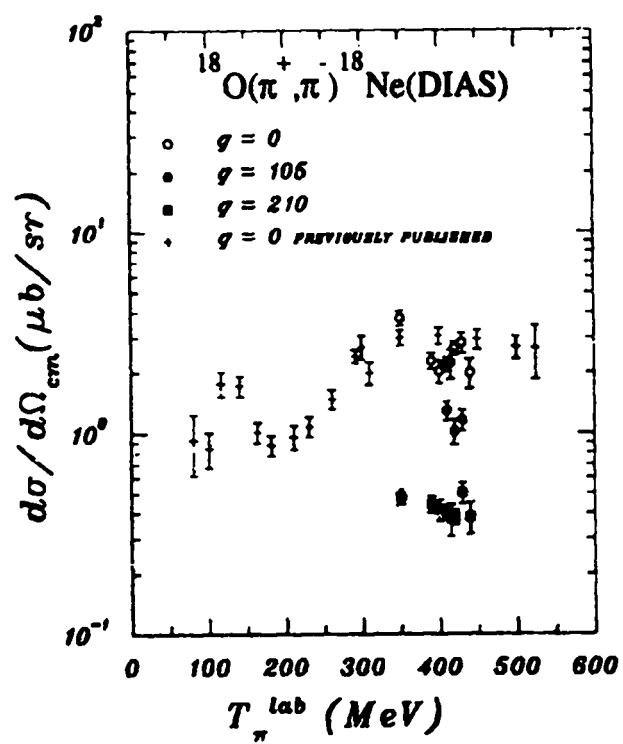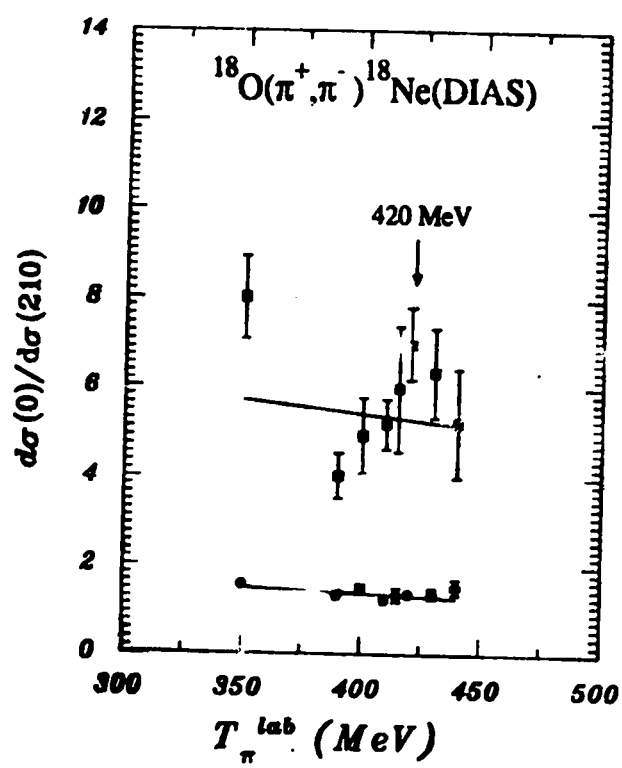
DIAS

$q = 210$ MeV/c

7 MeV   13 MeV

DIAS

Fig. 2

Fig. 3

BIBLIOGRAPHY

[Am-79] J. F. Amann *et. al.*, IEEE Trans. on Nucl. Science **NS-26**, 4389 (1979).

[Ar-83] R. Arndt, computer code SAID, Phys. Rev. D **28**, 97 (1983), Winter 1992 solutions.

[At-81] L. G. Attencio *et al.*, Nucl. Instrum. Methods **187**, 381 (1981)

[Be-69] Philip R. Bevington, *Data reduction and error analysis for the physical sciences*, (McGraw-Hill, New York, 1969).

[Bh-86] R. S. Bhalerao and L. C. Liu, Phys. Rev. Lett. **54**, 865 (1985).

[Bo-69] Aage Bohr and Ben R. Mottelson, *Nuclear Structure, vol. 1*, (W. A. Benjamin, New York, 1969).

[Ch-91] H. C. Chiang *et. al.*, Phys. Rev. C **44**, 738 (1991).

[Ch-88] R. E. Chrien *et. al.*, Phys. Lett. **60B**, 2595 (1988).

[Cl-82] P. Clout, Los Alamos National Laboratory report LA-UR-82-2718, Rev. III (1982).

[Ei-87] J. Eisenberg and D. Koltun, *Theory of Meson Interactions with Nuclei*, (John Wiley and Sons, New York, 1987).

[Ei-80] J. M. Eisenberg and W. Greiner, *Nuclear Theory*, (North-Holland, New York, 1980).

[Gi-85a] R. A. Gilman, Ph. D. thesis, University of Pennsylvania, Los Alamos report LA-10524-T (1985).

[Gi-85b] R. A. Gilman, in *Proceedings of the LAMPF Workshop on Pion Double Charge Exchange*, Los Alamos, NM, 1985, edited by H. W. Baer and M. J. Leitch (Los Alamos National Laboratory report LA-10550-C, 1985).

[Gr-81] S. J. Greene, Ph. D. thesis, University of Texas at Austin, Los Alamos report LA-8891-T (1981).

[Gr-82] S. J. Green *et. al.*, Phys. Rev. C **25**, 927 (1982) and P. A. Seidl *et. al.*, Phys. Lett. **154B**, 255 (1985).

[Ha-86] Q. Haider and L. C. Liu, Phys. Lett. **172B**, 257 (1986).

[Ha-87] Q. Haider and L. C. Liu, Phys. Rev. C **36**, 1636 (1987).

[Kin] M. Oothoudt, computer code KINREL, unpublished.

[La-84] *Lampf Users Handbook*, (Los Alamos National Laboratory report MP-DO-UHB(Rev.), 1984).

[Li-92] L. C. Liu, private communication (1992).

[Li-88] B. J. Lieb *et. al.* in Progress at LAMPF, 1988 (unpublished).

[Mag] M. Hoen, computer code MAG, unpublished.

[Mo-90] C. L. Morris, computer code MON90, unpublished.

[Mo-78] C. L. Morris, G. W. Hoffmann and H. A. Thiessen, IEEE Trans. on Nucl. Science **NS-25**, 141 (1978) and C. L. Morris and G. W. Hoffmann, Nucl. Instrum. Methods **153**, 599 (1978).

[Ne-82] Roger G. Newton, *Scattering theory of waves and particles*, (Springer-Verlag, New York, 1982).

[Od-91] J. M. O'Donnell, private communication (1991).

[P3E-87] E1028 development and P3E Manual, *Channel Setup and Operation* (1987).

[Pr-90] *Review of Particle Properties*, G. F. Bertsch *et al.*, eds., Phys. Lett. **B239**, II.4 (1990).

[Q-89] *Q System Programmer's Information Manual*, Los Alamos National Laboratory report. MP-1-3401-5 (1989).

[Ro-67] Leonard S. Rodberg and R. M. Thaler, *Introduction to the Quantum Theory of Scattering*, (Academic Press, New York, 1967).

[Se-85] P. A. Seidl, Ph. D. thesis, University of Texas at Austin, Los Alamos report LA-10338-T (1985).

[Sh-74] S. Shlaer, Los Alamos National Laboratory Report LA-5511-MS (1974).

[Ta-72] John R. Taylor, *Scattering theory: the quantum theory of nonrelativistic collisions*, (Wiley, New York, 1972).

[Wi-91] A. L. Williams, Ph. D. thesis, University of Texas at Austin, Los Alamos report LA-12209-T (1991).

[Wi-89] A. L. Williams *et. al.*, Phys. Lett. **216B**, 11 (1989).

[Yu-35] H. Yukawa, Proc. Phys. Math. Soc. Japan **17**, 48 (1935).